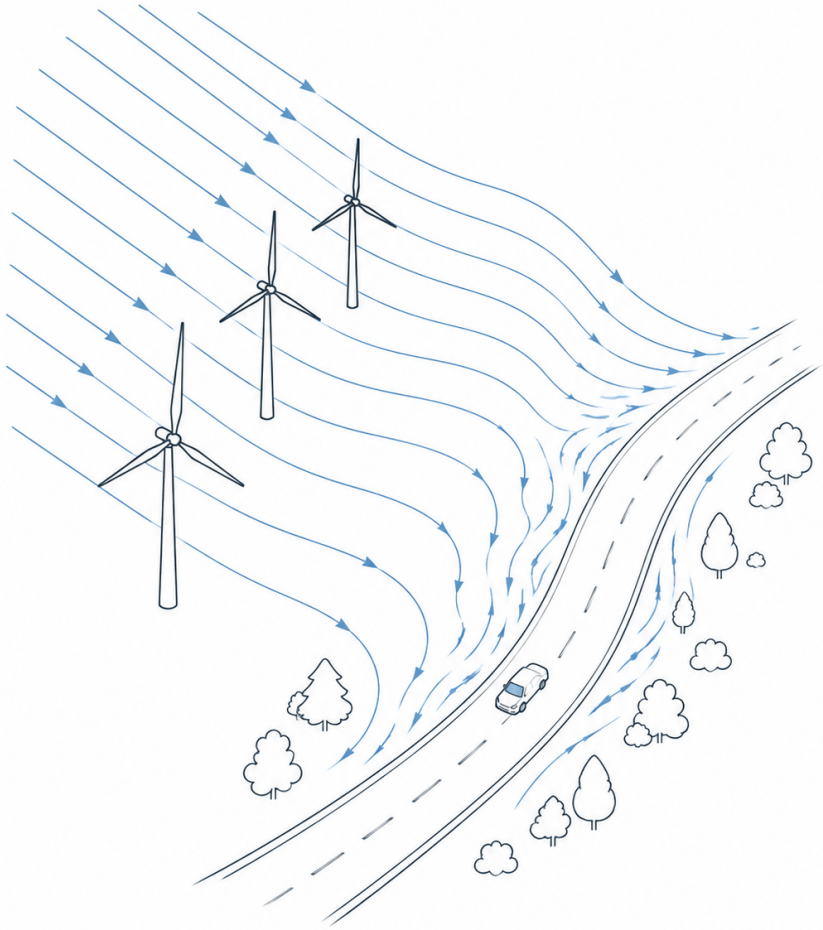
CHALMERS
UNIVERSITY OF TECHNOLOGY



Road Section Weather and Vehicle Energy Consumption Modeling

Master's thesis in Systems, Control and Mechatronics and
Infrastructure and Environmental Engineering

Otto Eriksson
Kaiyuan Liu

DEPARTMENT OF ELECTRICAL ENGINEERING
CHALMERS UNIVERSITY OF TECHNOLOGY
Gothenburg, Sweden 2026
www.chalmers.se

Master's thesis 2026

Road Section Weather and Vehicle Energy Consumption Modeling

Otto Eriksson
Kaiyuan Liu



CHALMERS
UNIVERSITY OF TECHNOLOGY

Department of Electrical Engineering
Division of Systems and Control
Chalmers University of Technology
Gothenburg, Sweden 2026

Road Section Weather and Vehicle Energy Consumption Modeling
Otto Eriksson
Kaiyuan Liu

© Otto Eriksson, Kaiyuan Liu 2026.

Supervisor: Mikael Askerdal, Volvo Group Trucks Technology & Industrial Division
Examiner: Jonas Fredriksson, Department of Electrical Engineering

Master's Thesis 2026
Department of Electrical Engineering
Division of Systems and Control
Chalmers University of Technology
SE-412 96 Gothenburg
Telephone +46 31 772 1000

Cover: Wind visualization showing how regional wind can evolve into local roadside wind.

Typeset in LaTeX
Gothenburg, Sweden 2026

Abstract

Accurate vehicle energy consumption modeling for heavy-duty trucks requires precise characterization of aerodynamic drag and rolling resistance, both of which are highly sensitive to local weather and road conditions. Existing models often rely on standard atmospheric assumptions or dedicated on-board sensors, which limits their ability to capture real-world operating conditions. To address this, the present work proposes an integrated physics-based modeling framework that links road-segment-level meteorological data to vehicle motion resistance without requiring additional sensing hardware.

For the wind prediction model, a topographical model is used as a base and further corrected with a two-layer wind speed correction model developed to translate regional meteorological station measurements into local road-level wind estimates. The successive layers account for a global power law bias and geographic environment effects through clustering of road segments into sheltered and wind-amplified categories. Validated against over 200 repeated real-world journeys on RV (Riksväg) 40, Sweden, the model achieves a 48.4% reduction in mean absolute error over the regional baseline, consistently across seasons and travel directions, compared to using measurements from regional meteorological stations. A wind direction model in the form of a polynomial is incorporated to complete the wind characterization.

For the rolling resistance component, a two-state tire thermodynamic observer is formulated, estimating tire bulk temperature from standard Tire Pressure Monitoring System (TPMS) measurements and an external temperature sensor via a Kalman filter. This enables model-based prediction of temperature-dependent rolling resistance as a function of ambient conditions and driving dynamics, without dedicated thermal sensors.

The proposed framework provides a scalable, low-cost approach to weather-aware energy consumption forecasting, directly applicable to range prediction and route planning for heavy-duty trucks operating under dynamic real-world road section conditions.

Keywords: Meteorological Data, Motion Resistance, Vehicle Energy Consumption

Acknowledgements

We would like to express sincere gratitude to our examiner Jonas Fredriksson and our supervisor Mikael Askerdal for their guidance and continuous support in the thesis work.

We are also thankful for the opportunity to carry out this project at Volvo Group. We thank the responsible people for the AutoFreight 2 data gathering project as well as Reno Filla at Scania for the cooperative data exchange.

Finally, we are grateful to our families, schoolmates, examiners at Chalmers and colleagues at Volvo Group for encouragement, help and the ability to graduate at Chalmers University of Technology.

Otto Eriksson and Kaiyuan Liu, Gothenburg, June 2026

List of Acronyms

Below is the list of acronyms that have been used throughout this thesis listed in alphabetical order:

CAN	Controller Area Network
CFD	Computational Fluid Dynamics
GIS	Geographic Information System
GPS	Global Positioning System
ICC	Intraclass Correlation Coefficient
LOO-CV	Leave-One-Out Cross-Validation
LPV	Linear Parametric Variable
MAE	Mean Absolute Error
RV	Riksväg
SMHI	Swedish Meteorological and Hydrological Institute
SR	Shelter Ratio
TPMS	Tyre Pressure Monitoring System

Nomenclature

Below is the nomenclature of indices, parameters, and variables that have been used throughout this thesis.

Indices

k	Segment index
i	trip index
c	Cluster index

Parameters

c_{IJ}	Coefficients governing heat transfer
m_{t2}	Total mass of T_{TB} state
c_{t2}	Heat capacity for T_{TB}
m_{ta}	Total mass of cavity air
c_{ta}	Heat capacity of cavity air
V	Tire cavity air volume
N	Moles of air
R	Universal gas constant
$a,\ b$	Power law correction coefficients
V^*	Power law crossover wind speed
N_k	Number of trips observing segment k

Variables

F_{air}	Air resistance
F_{roll}	Rolling resistance

F_{grad}	Gradient resistance
F_{acc}	Inertial resistance
ρ	Air density
C_d	Aerodynamic drag coefficient
A	Effective frontal area
v_{rel}	Relative wind speed
α	Relative wind direction
C_{rr}	Rolling resistance coefficient
m	Mass
g	Gravitational acceleration
ϕ	Road slope angle
v_v	Vehicle speed
v_w	Absolute wind speed
θ	Absolute wind direction
v_{wCross}	Absolute crosswind speed
v_{wHead}	Absolute headwind speed
V_{SMHI}	SMHI background (regional) wind speed
θ_{SMHI}	SMHI background (regional) wind direction
V_{anem}	Anemometer-measured local wind speed
$\hat{V}_{L1}(k,i)$	Layer 1 predicted wind speed for segment k during trip i
$\hat{V}_{L2}(k,i)$	Layer 2 predicted wind speed for segment k during trip i
$\hat{V}_{L3}(k,i)$	Layer 3 predicted wind speed for segment k during trip i
$f(V_{\text{SMHI}})$	Power law correction factor
Δ_c	Cluster-level mean residual (Layer 2 correction)
$\varepsilon(k,i)$	Layer 2 residual of segment k on trip i
β	Vehicle yaw angle
c	Cluster
SR	Shelter ratio
$SR(k,i)$	Shelter ratio for road segment k during trip i
$\overline{SR}_k$	Mean shelter ratio for road segment k
Δ_c	Cluster-level mean residual correction after Layer 1
$\mathcal{K}_c$	Set of road segments assigned to cluster c
μ_{resid}	Mean residual
T_T	Tire temperature

T_{RS}	Road surface temperature
c_{RS}	Road surface condition
T_{TB}	Tire bulk average temperature
T_{TA}	Tire cavity air temperature
P_{rr}	Hysteresis loss
T_a	Ambient air temperature
p_T	Tire pressure
$\bar{h}$	Average altitude of road section
$\bar{H}$	Average altitude of perception box
x	Tyre temperature state vector
u	Observer input (rolling resistance power)
d	Disturbance vector
$A,\ B,\ C,\ F$	State-space system matrices
K_k	Kalman gain
P	State estimate covariance matrix
Q	Process noise covariance matrix
R_k	Measurement noise covariance matrix

Contents

List of Acronyms **ix**

Nomenclature **xi**

List of Figures **xvii**

List of Tables **xxi**

1 Introduction **1**
1.1 Background . . . 1
1.2 Problem Statement . . . 3
1.3 Objective . . . 3
1.4 Outline . . . 4
1.5 Limitations . . . 5
1.6 Sustainability Aspects . . . 5

2 Theory **7**
2.1 Vehicle Resistance Modeling . . . 7
2.1.1 Aerodynamic Drag Modeling . . . 7
2.1.2 Rolling Resistance Modeling . . . 8

3 Methods **11**
3.1 Data Sources . . . 11
3.1.1 Vehicle Operational Data . . . 11
3.1.2 Meteorological Data . . . 12
3.1.3 Geographical Data . . . 14
3.1.4 Route Description . . . 16
3.2 Absolute Wind Calculation . . . 16
3.3 Wind Sensor Calibration . . . 17
3.3.1 Wind Direction Alignment Calibration . . . 17
3.3.2 Wind Data Calibration . . . 18
3.4 Wind Data Analysis . . . 19
3.4.1 Road Segmentation . . . 19
3.4.2 Wind Angle Sections . . . 19
3.4.3 Topography Analysis . . . 20
3.4.4 Landscape Analysis . . . 21
3.4.4.1 Layer 1: Global Correction . . . 23

3.4.4.2 Layer 2: Wind-behavior Cluster Correction 25
3.4.4.3 Layer 3: Segment Residual Correction 27
3.4.4.4 Model Evaluation 28
3.4.5 Wind Direction Model 30
3.5 Rolling Resistance Modeling 30
3.5.1 Two-State Tire Temperature Observer 30

4 Results **35**
4.1 Wind Data Calibration 35
4.1.1 Alignment Error 35
4.1.2 Data Calibration 35
4.2 Wind Models 37
4.2.1 Topographic Model 37
4.2.2 Landscape Wind Model 37
4.2.2.1 Three-Layer Wind Speed Correction Model 37
4.2.2.2 Layer 1: Global Correction 39
4.2.2.3 Layer 2: Wind-Behavior Cluster Correction 40
4.2.2.4 Road Segments Land-Cover Analysis 42
4.2.2.5 Layer 3: Segment Residual Correction 46
4.2.2.6 Model Validation and Generalization 47
4.2.3 Integrated Model 49
4.2.4 Wind Direction Model 49
4.3 Rolling Resistance 50
4.3.1 Rolling Resistance Model 51
4.3.2 Rolling Resistance Model with Observer 52

5 Conclusion **55**

Bibliography **57**

A Appendix 1 **I**

List of Figures

1.1 Overview of the thesis framework. 4

2.1 Visual representation of equation components affected by wind. . . . 8

3.1 Local segment-level wind speed compared with the SMHI station wind speed along a single trip. The stepped SMHI signal reflects its hourly resolution. 13
3.2 Wind rose comparing the SMHI station wind direction with the local segment-level wind direction for the same trip as Figure 3.1. 13
3.3 Headwind and crosswind components of the local wind along the route for the same trip as Figure 3.1. A positive headwind opposes the direction of travel. 14
3.4 Example visualisation of the land-cover polygons provided in *Marktäcke Nedladdning, vektor*. Source: © Lantmäteriet. 15
3.5 Example visualisation of the building-footprint polygons provided in the *Byggnad Nedladdning, vektor* dataset. Source: © Lantmäteriet. . 15
3.6 Transport route between Gothenburg and Viared used in the vehicle measurement data. 16
3.7 Visualization of headwind and crosswind components. 17
3.8 Truck used for data collection and calibration. 18
3.9 Sectioning of wind data. 20
3.10 Perception box of elevation area. 21
3.11 Relationship between trip-mean shelter ratio SR_i and SMHI background wind speed $V_{\mathrm{SMHI},i}$ for the 143 analyzed trips. The solid curve represents the fitted power-law relationship used for the Layer 1 global correction. 24
3.12 Visualization of temperatures. 31
3.13 Block diagram of tire temperature model. 32
3.14 Block diagram of model with Kalman filter. 33

4.1 Results of calibration for the average of all trips. 36
4.2 Results of calibration with high wind visor setting. 36
4.3 LOO-CV MAE for each model layer. 38

4.4 Prediction for one randomly selected trip from the 143 valid trips. Upper panel: SMHI background wind speed, measured anemometer wind speed, and three-layer model prediction along the RV 40 route. Lower panel: prediction error for the SMHI baseline and the three-layer model. 39
4.5 Spatial distribution of wind-behavior clusters along RV 40. 40
4.6 Distribution of segment-mean shelter ratio SR by cluster. 41
4.7 Land cover composition along a trip, aggregated into 500 m distance bins. Area fractions are computed within a 250 m radius buffer around each segment centre from Lantmäteriet Marktäcke data. 42
4.8 Overview of road-segment classification in the main land-cover type of the route from Gothenburg to Borås. 43
4.9 Dominant land-cover type assigned to each 500-meter road segment around the Gothenburg city area. 44
4.10 Dominant land-cover type assigned to each 500-meter road segment along the highway from Landvetter Airport to Borås. 44
4.11 Shelter ratio of individual road-segment observations along the route, stratified by segment type. (a) All $n = 18{,}678$ valid segment–trip observations from 143 trips in both travel directions. (b) Median (black line) and interquartile range (shaded bar) of SR for each segment type, with the 75th percentile, median, and 25th percentile given numerically. Segment types are defined by areal dominance ($\geq 50\%$) of the corresponding land-cover class within the segment buffer; segments without a dominant class are labeled Mixed. 45
4.12 Segment-level mean residuals after Layer 2 correction, plotted against distance from Gothenburg. 47
4.13 (a) Kernel density estimates of prediction error for the SMHI baseline and three-layer model. (b) Mean absolute error stratified by SMHI wind speed bin. 48
4.14 (a) Monthly LOO-CV MAE for the SMHI baseline and three-layer model. Error bars indicate one standard deviation across trips within each month. (b) Monthly improvement of the three-layer model over the SMHI baseline. 48
4.15 Results for models in the angle section around 90 degrees. 49
4.16 Polynomial comparison for wind direction model. 50
4.17 Cold dry trip. 51
4.18 Hot dry trip. 51
4.19 Cold wet trip. 52
4.20 Hot wet trip. 52
4.21 Cold dry trip with KF. 52
4.22 Hot dry trip with KF. 52
4.23 Cold wet trip with KF. 53
4.24 Hot wet trip with KF. 53

A.1 Results for models in angle section around 0 degrees. I
A.2 Results for models in angle section around 30 degrees. II

A.3 Results for models in angle section around 60 degrees. II
A.4 Results for models in angle section around 120 degrees. III
A.5 Results for models in angle section around 150 degrees. III
A.6 Results for models in angle section around 180 degrees. IV
A.7 Results for models in angle section around 210 degrees. IV
A.8 Results for models in angle section around 240 degrees. V
A.9 Results for models in angle section around 270 degrees. V
A.10 Results for models in angle section around 300 degrees. VI
A.11 Results for models in angle section around 330 degrees. VI

List of Tables

3.1 Mapping from Lantmäteriet Marktäcke categories to the four land cover classes used in this study. Data from Byggnad Nedladdning and Marktäcke Nedladdning, vektor. 27

4.1 LOO-CV mean absolute error (MAE) for each model layer. 38
4.2 Mean land-cover area fractions within a 250 m buffer around road segments, aggregated into 5km distance bins along RV 40. 42
4.3 Absolute errors by angle (rounded to 2 decimals). 50
4.4 Section angle and measured angle. 51

1

Introduction

1.1 Background

Road-section emissions account for a significant share of global energy consumption and greenhouse gas emissions [1], making efficient and accurate vehicle energy management crucial to achieving sustainable mobility. For large vehicles typically used in commercial transport, the limited range and the need for on-time delivery are primary trade-offs, as increasing speed to improve the probability of meeting time requirements may reduce range and the likelihood of reaching the final destination or a charging point, and vice versa [2]. Therefore, accurate energy consumption prediction, such as range prediction, route planning, charging strategies, and energy management, is essential for these types of vehicles. Recent years have seen dedicated efforts to develop physics-based and data-driven models to predict vehicle energy consumption, applied to electric vehicle range estimation and real-time energy management [3] [4]. Martini et al. [5] evaluated various energy consumption models using real-world driving data. The model incorporating detailed drag components and a constant efficiency factor showed the highest prediction accuracy across all metrics. Furthermore, combining physical models with machine learning can improve prediction accuracy [6].

Most existing approaches simulate vehicle dynamics by decomposing total traction into aerodynamic drag, rolling resistance, gravitational drag, and inertia components, [7]. Among these factors, aerodynamic drag and rolling resistance constitute the primary resistive forces during high-speed steady-state operation, exhibiting high sensitivity to weather and environmental factors, [8]. In representative test cycles in the EU and the United States, aerodynamics accounts for approximately 15–20% of total energy losses for heavy-duty vehicles, [9]. Likewise, reducing rolling resistance is recognized as an effective way to improve vehicle energy efficiency. For example, low rolling-resistance tires can reduce fuel consumption in U.S. trucks by about 3% while the use of single-wide tires in lieu of traditional dual tire sets on truck rear axles and trailer axles can reduce fuel use by up to 9%, [10].

Aerodynamic drag mainly arises from pressure drag caused by the vehicle displacing the oncoming air and from friction drag along the vehicle surface. Ambient wind alters the relative airflow around the vehicle, while crosswinds can increase the aerodynamic yaw angle and thereby substantially influence both drag and lateral

aerodynamic forces. Studies have shown that a vehicle's total drag typically peaks within a yaw angle range of 20–40°, while lateral forces increase approximately linearly with yaw angle when the yaw angle is less than 60° [11–13]. Aerodynamic drag is typically modeled as a function of air density, frontal area, drag coefficient, and the relative air velocity between the vehicle and the surrounding airflow. The frontal area and drag coefficient are vehicle-specific, while air density and relative air velocity depend on meteorological conditions, including wind speed, wind direction, temperature, humidity, and atmospheric pressure. Previous research indicates that headwinds and tailwinds significantly increase aerodynamic drag and vehicle energy consumption, particularly for heavy vehicles and at high speeds [2]. Existing energy consumption models often simplify assumptions to standard atmospheric conditions or rely on vehicle-mounted wind sensors, limiting their ability to account for spatially and temporally varying weather conditions across routes when onboard measurements are unavailable.

Rolling resistance is typically modeled as proportional to the normal load, using a rolling resistance coefficient. However, the rolling resistance coefficient depends on several factors, and numerous experimental studies have demonstrated significant correlations between rolling resistance and tire temperature, tire pressure, road surface conditions, and vehicle load; see, e.g., [14] [15]. Among these, tire temperature plays a critical role. At lower temperatures, the internal hysteresis loss cycle increases, thereby increasing rolling resistance, whereas higher temperatures reduce internal energy dissipation [16]. Recent studies have examined the effects of operating and environmental conditions on tire temperature, as well as the resulting influence of tire temperature on rolling resistance and vehicle energy consumption [17–19]. However, research on the relationship between real-world driving weather data and tire thermodynamics remains insufficient.

This thesis aims to develop an integrated framework that links road-segment-level meteorological conditions to vehicle energy consumption through physics-based models of aerodynamic drag and rolling resistance. For the aerodynamic component, this thesis investigates the relationship between meteorological station observations and the wind conditions vehicles experience along different road-segment types. The objective is to map weather-station-level wind data to road-segment-level wind conditions and, subsequently, to aerodynamic drag, enabling more accurate segment-level energy consumption estimates without relying on dedicated onboard wind measurements. Road segments are classified according to their geometric, environmental, and meteorological characteristics to investigate the relationship between wind conditions at meteorological stations and road segments. For the rolling resistance component, a tire temperature state model examines how ambient temperature, road surface temperature, vehicle speed, and vehicle load influence tire temperature and, consequently, rolling resistance and energy consumption. In general, the proposed framework aims to improve the physical interpretability and spatial resolution of weather-dependent vehicle energy consumption models.

1.2 Problem Statement

A major challenge in vehicle energy consumption modeling is the influence of weather conditions. Factors such as ambient temperature, precipitation, and wind substantially affect motion resistance, particularly air drag and rolling resistance. While existing models describe these effects using weather parameters, they are often developed under controlled conditions or based on generalized assumptions. As a result, they do not fully capture the complex and highly local nature of real road weather. A key technical challenge is characterizing wind effects. Roadside wind measurements are sparse and subject to strong local variations caused by terrain, vegetation, buildings, and traffic. Interpolating wind conditions between measurement points is therefore highly uncertain. Even small differences in wind and temperature can significantly increase energy consumption.

The proposed modeling framework integrates external weather conditions and vehicle operational data to compute physics-based motion resistances, specifically aerodynamic drag (F_{air}) and rolling resistance (F_{roll}), which could subsequently be fed into the vehicle energy consumption models.

1.3 Objective

This thesis aims to develop a physics-based framework that links road-segment-level meteorological conditions to vehicle motion resistance and energy consumption. The framework comprises two main components: the aerodynamics section integrates regional meteorological observation data and vehicle measurement data to estimate the wind conditions the vehicle experiences on road segments. The rolling resistance component uses a thermodynamic tire temperature model to estimate the tire's internal temperature based on ambient temperature, road surface temperature, vehicle operating conditions, and available tire pressure monitoring system (TPMS) measurements, and to model rolling resistance. Together, these two components provide more accurate inputs for the vehicle energy consumption model. Consequently, the main research questions of this study are as follows:

1. How does the local weather on the road relate to the regional weather, and how are these relationships affected by local geographic and environmental characteristics?

2. To what extent can a simple local correction model using map-based features improve the estimation of local wind conditions from meteorological observations compared with the regional wind data?

3. To what extent can a tire thermal model estimate tire bulk temperature and support temperature-dependent rolling resistance modeling under different ambient temperatures and road surface conditions?

1.4 Outline

The overall structure of this thesis is shown in Figure 1.1. The framework uses three data sources: vehicle operation data measured onboard (anemometer, CAN bus, and tire pressure monitoring system signals), geographic data from open sources and meteorological data from regional weather stations.

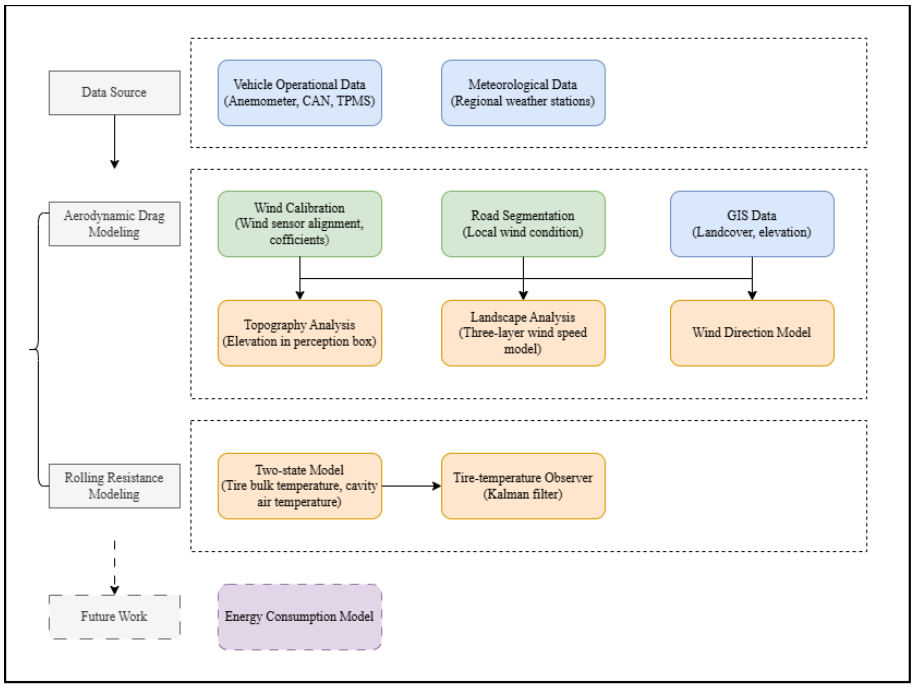


Figure 1.1: Overview of the thesis framework.

The data is input into two parallel modeling tasks, corresponding to the two motion resistance components discussed earlier. The first task models aerodynamic drag. First, the wind sensor signals are calibrated to determine the sensor offset and calibration coefficients. Second, in the road segmentation step, the route is divided into discrete segments at fixed 500-meter intervals to correlate local wind conditions with specific locations. Then, three sub-models are combined: terrain analysis, which correlates local wind with elevation differences within the sensing frame; landscape analysis, which constructs a three-layer wind speed model; and a wind direction model, which maps regional wind direction to local wind direction along the road. The second task is rolling resistance modeling, which uses a two-state thermodynamic model of tire bulk temperature and cavity air temperature, along with a Kalman filter-based tire temperature observer, to estimate the temperature-dependent rolling drag coefficient.

The outputs of these two branches are intended to serve as inputs to the vehicle energy consumption model. Complete energy consumption calculations and related range predictions are beyond the scope of this thesis and are marked as future work in Figure 1.1.

1.5 Limitations

This study faces certain objective limitations in its implementation and modeling process, primarily manifested in the following aspects:

First, because of the 20-week project timeline and data collection scope, the measured vehicle data primarily comes from a single fixed route between Gothenburg harbor and Viared. This spatial limitation means the model covers relatively homogeneous terrain features and road conditions. To generalize to broader, more complex geographical environments requires further validation.

Second, onboard sensor constraints introduced measurement uncertainties. For aerodynamic measurements, onboard wind speed sensors inevitably suffered interference from flow-field distortions caused by the truck's aerodynamic shape. Coupled with potential deviations in installation alignment, this requires rigorous calibration of raw data before use. Regarding rolling resistance, existing tire sensors cannot directly measure resistance values, requiring model-based conversion from indirect physical quantities, a process inherently carrying unavoidable errors.

Finally, model assumptions involve compromises with external environmental data. On the one hand, historical road-segment meteorological data still lack sufficient spatiotemporal resolution and completeness, making it difficult to fully capture transient local microclimate changes. On the other hand, wind field modeling is constrained by complex traffic environments. Given the limited research on how upstream vehicle wakes affect the aerodynamic drag of following vehicles, this study adopts a simplified modeling assumption and disregards the interference of surrounding traffic flow on local wind conditions.

1.6 Sustainability Aspects

From a sustainability perspective, the goal is to use resources efficiently, reduce environmental impact, and ensure long-term viability. Efforts are made to optimize processes to reduce waste, energy consumption, and emissions. Sustainable practices are integrated into the design and implementation stages to sustain the project's benefits over time without compromising future needs. This project relates to United Nations SDG 9 (Industry, Innovation and Infrastructure), 12 (Responsible Consumption and Production), 13 (Climate Action) and 16 (Peace, Justice and Strong Institutions).

2

Theory

This section clarifies the aerodynamic model and the thermodynamic rolling resistance model, incorporating these meteorological factors. Therefore, accurately modeling vehicle energy consumption under varying weather conditions requires incorporating these effects into the resistance models. This section clarifies the aerodynamic model and the thermodynamic rolling resistance model, with particular emphasis on how meteorological factors are incorporated.

2.1 Vehicle Resistance Modeling

The total longitudinal traction force demand of a vehicle is typically decomposed into four primary resistance components: aerodynamic drag (F_{air}), rolling resistance (F_{roll}), gradient resistance (F_{grad}), and inertial resistance (F_{acc}). The fundamental longitudinal dynamics equation can be expressed as:

$$F_{trac} = F_{air} + F_{roll} + F_{grad} + F_{acc} \tag{2.1}$$

where the resistance to the gradient is related to the level of the road, and the inertial resistance is associated with acceleration. Under cruising or steady-state driving conditions, aerodynamic drag and rolling resistance are the predominant sources of energy consumption, both of which are highly sensitive to meteorological and environmental conditions.

2.1.1 Aerodynamic Drag Modeling

Traditional energy consumption models often assume still atmospheric conditions, implying that the relative wind speed equals the vehicle speed. However, in actual driving scenarios, ambient wind (both speed and direction) significantly alters the vehicle's effective frontal area and aerodynamic characteristics. The aerodynamic drag accounting for ambient wind fields can be modeled as:

$$F_{air} = \frac{1}{2}\rho C_d A v_{rel}^2 \tag{2.2}$$

where ρ is the air density, A is the effective frontal area of the vehicle, $C_d(\alpha)$ is the aerodynamic drag coefficient dependent on the yaw angle α, and v_{rel} is the relative air speed between the vehicle and the surrounding air.

The relative air velocity is determined by the vector difference between the vehicle velocity and the ambient wind velocity. Thus, both wind speed and wind direction influence the aerodynamic load. If the vehicle velocity vector is denoted by $\mathbf{v}_v$ and the wind velocity vector by $\mathbf{v}_w$, the relative wind velocity can be expressed as

$$\mathbf{v}_{rel} = \mathbf{v}_w - \mathbf{v}_v. \tag{2.3}$$

and its magnitude is given by

$$v_{rel} = |\mathbf{v}_{rel}|\,. \tag{2.4}$$

The direction of the relative wind determines the yaw angle α, which in turn affects the aerodynamic drag coefficient. §

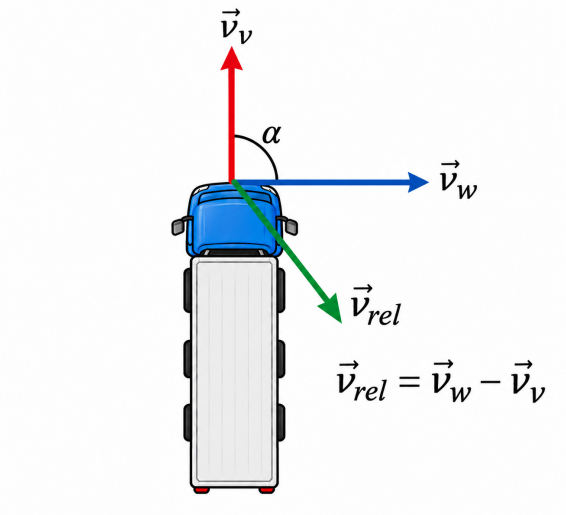


Figure 2.1: Visual representation of equation components affected by wind.

Headwind increases the relative air velocity and therefore the aerodynamic drag, while a tailwind has the opposite effect. Crosswinds primarily influence the yaw angle and may consequently alter the aerodynamic drag coefficient. The effect of wind direction therefore depends on the relative orientation between the vehicle and the wind.

2.1.2 Rolling Resistance Modeling

The rolling resistance coefficient is strongly affected by the tire rubber's viscoelastic behavior. As tire temperature increases, the internal hysteresis losses in the rubber compound decrease, reducing rolling resistance. Conversely, low temperatures increase the rubber's stiffness, increasing rolling resistance.

Since the vehicle data do not include direct tire temperature measurements, a tire temperature estimation approach is required. The fundamental rolling resistance equation can be expressed as:

$$F_{roll} = C_{rr} mg \cos(\phi) \tag{2.5}$$

where C_{rr} is the rolling resistance coefficient, m is the vehicle mass, g is the acceleration of gravity and ϕ is the road slope angle. In winter operating conditions, tire temperature is influenced not only by internal heat generation from cyclic deformation but also by heat exchange with the road surface and the surrounding environment. Consequently, the rolling resistance coefficient can be considered a function of both tire temperature and road surface conditions

$$C_{rr} = f(T_T, T_{RS}, c_{RS}) \tag{2.6}$$

where T_T represents the tire temperature, T_{RS} is the road surface temperature, and c_{RS} denotes the road surface condition (e.g., dry asphalt, wet surface, or snow/ice).

Tire temperature cannot be assumed to equal ambient temperature, since it evolves dynamically due to heat generation within the tire and heat exchange with its surroundings. The main source of internal heat generation is tire deformation during rolling, while heat is dissipated through heat transfer to the surrounding air and the road surface. Vehicle speed also affects the rates of heat generation and heat transfer.

The thermal behavior can generally be described as an energy balance between internally generated heat and heat transferred from the tire to its surroundings. A simplified representation can be written as

$$C_T \frac{\mathrm{d}T_T}{\mathrm{d}t} = \dot{Q}_{\mathrm{gen}} - \dot{Q}_{\mathrm{air}} - \dot{Q}_{\mathrm{road}}. \tag{2.7}$$

where C_T represents the effective thermal capacity of the tire, $\dot{Q}_{gen}$ is the heat generated by tire deformation, and $\dot{Q}_{air}$ and $\dot{Q}_{road}$ represent heat transfer to the surrounding air and road surface, respectively.

Ambient air temperature affects the thermal model through the temperature difference between the tire and the surrounding air, thereby influencing convective heat transfer. Similarly, road-surface temperature affects heat exchange between the tire and the road. A cold road surface can increase the rate at which heat is removed from the tire, while a warmer road surface reduces this cooling effect. Vehicle speed influences the thermal model through both the rate of tire deformation and the heat transfer to the surrounding air.

Road-surface condition is particularly relevant during the winter. Dry asphalt, wet asphalt, snow, and ice can produce different tire-road interaction characteristics and, therefore, different rolling resistance. Consequently, road-surface temperature should be considered alongside surface condition, rather than treated as an independent temperature effect.

3

Methods

3.1 Data Sources

This study's analysis is based on three main databases: vehicle operational data from a freight truck, meteorological data from roadside weather stations, and geographic data from open sources. These datasets were combined to investigate the relationship between local road weather conditions and vehicle motion resistance.

3.1.1 Vehicle Operational Data

Volvo Group Trucks Technology provided the vehicle data, which consists of operational measurements collected from a freight truck operating along a fixed transport route between the Port of Gothenburg and Viared, Sweden. The data collection campaign was conducted as part of the *Autofreight 2* research project. The data were received in CSV files for each trip without preprocessing.

The test vehicle was a Volvo FH 4×2 tractor equipped with a fully electric powertrain consisting of four induction motors for traction. No trailer was attached during the measurements to simplify the analysis of the vehicle's motion resistance. The total vehicle mass during the tests was approximately 9000 kg.

The vehicle was equipped with several sensors to measure environmental and vehicle dynamic variables. A two-dimensional ultrasonic anemometer (Thies CLIMA) was mounted 40 centimeters above the cab to measure the relative wind speed and wind direction experienced by the vehicle. In addition, the vehicle was equipped with a Tire Pressure Monitoring System (TPMS) provided by Goodyear, which measures tire pressure and the temperature near the tire rim.

Additional signals recorded in the vehicle CAN data include vehicle speed, heading direction, traction power, and other operational variables required for motion resistance analysis.

To synchronize measurements from different sensors, the signals were aligned using timestamp matching and interpolation. After synchronization and quality filtering, 143 valid trips covering both travel directions were retained for the wind-model development and evaluation, corresponding to 18,678 valid segment-level observations. A trip was considered valid when the vehicle followed the predefined primary study

route and the required vehicle and meteorological signals were available continuously for the relevant analysis period. Observations containing missing or invalid vehicle or weather data were excluded.

3.1.2 Meteorological Data

To complement the vehicle measurements, meteorological data were obtained from roadside weather stations operated by the Swedish Transport Administration (Trafikverket) and SMHI (Sveriges meteorologiska och hydrologiska institut). Scania provided the weather station data, which correspond to stations along the truck's driving route.

The dataset includes hourly measurements of several meteorological variables relevant to vehicle energy consumption and aerodynamic resistance. In particular, the following variables were used in this study:

- Wind speed
- Wind direction
- Ambient air temperature
- Road surface temperature

We obtained the wind data from three SMHI weather stations located near Gothenburg, Landvetter Airport, and Borås. For each trip, the regional weather data were matched according to the vehicle position and measurement time. The station used for a given observation was selected to provide the most spatially and temporally representative background wind condition along the route. Consequently, the matched SMHI signal may change between stations during a single trip. A randomly selected trip is used as an example in Figures 3.1–3.3.

Throughout the subsequent wind analysis, two wind datasets are distinguished. The term *local wind* refers to the road-level absolute wind reconstructed from the vehicle-mounted anemometer measurements after wind-direction alignment, absolute-wind calculation, and sensor calibration. These measurements therefore represent the wind conditions the truck experienced locally at each road-segment observation.

The term *regional background wind* refers to the matched SMHI weather-station measurement associated with the same vehicle observation. It is used as the regional meteorological reference against which the calibrated local road-level wind is compared.

The analysis therefore compares a calibrated local road-level wind observation with a corresponding regional background wind reference for each segment–trip observation.

Figure 3.1 shows local wind speeds (calibrated vehicle operational data) along the route alongside wind speeds at the SMHI weather stations (meteorological data).

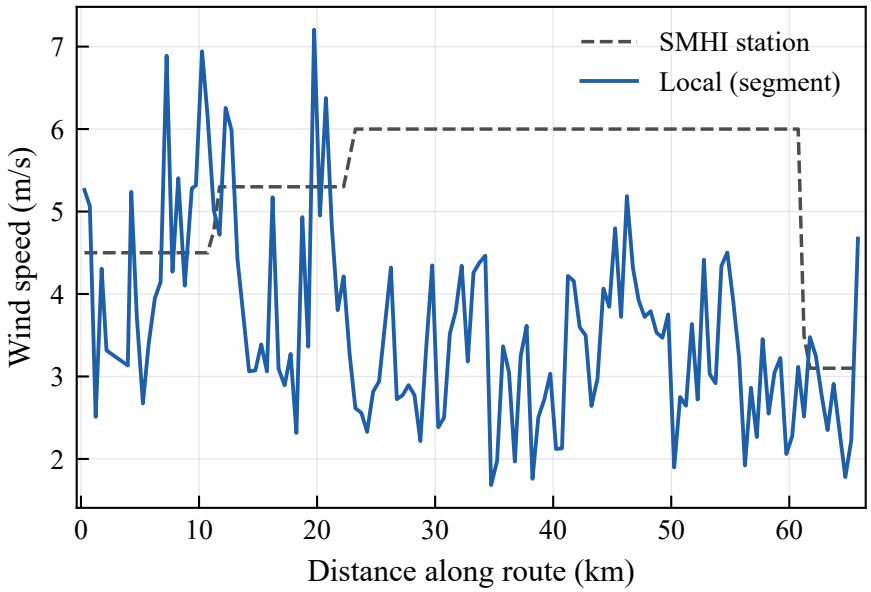


Figure 3.1: Local segment-level wind speed compared with the SMHI station wind speed along a single trip. The stepped SMHI signal reflects its hourly resolution.

Because SMHI wind speeds are reported hourly, their signal is relatively constant, while local wind speeds fluctuate significantly across road segments.

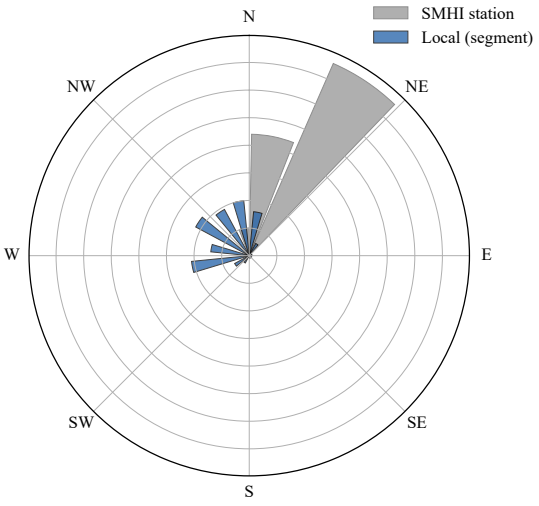


Figure 3.2: Wind rose comparing the SMHI station wind direction with the local segment-level wind direction for the same trip as Figure 3.1.

Figure 3.2 shows the wind direction distribution along the same route in the form of a wind rose diagram, showing the wind direction at the SMHI weather station with the local wind direction at each route segment. Although the two distributions share a dominant sector, significant differences in local directions reflect the influence of topography and surface cover on near-route airflow.

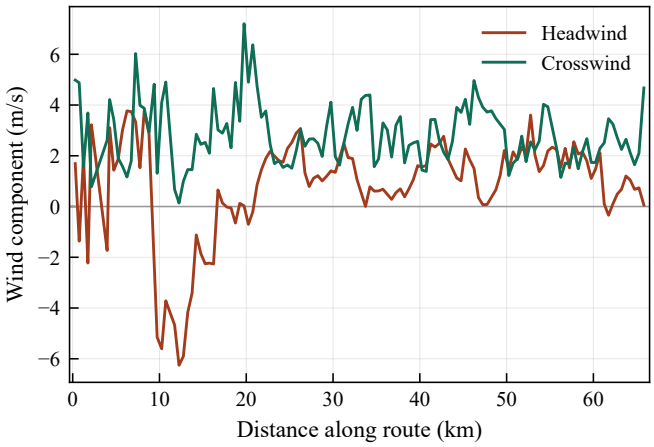


Figure 3.3: Headwind and crosswind components of the local wind along the route for the same trip as Figure 3.1. A positive headwind opposes the direction of travel.

Figure 3.3 decomposes the local wind along the route into headwind and crosswind components, where the positive and negative wind directions are opposite to the direction of travel. These two components vary significantly over a single trip. By definition, the crosswind component is non-negative and, on average, is comparable to the tailwind component, highlighting the importance of crosswinds for aerodynamic drag and prompting us to treat wind direction separately in the modeling.

3.1.3 Geographical Data

Geographic data were obtained from Lantmäteriet to characterize the local environment around each road segment. Three geographic data products were used: land-cover data from *Marktäcke Nedladdning, vektor* [20], building-footprint data from *Byggnad Nedladdning, vektor* [21], and terrain-elevation data from *Markhöjdmodell Nedladdning* [22]. The elevation model provides terrain data on a regular grid with a spatial resolution of 1×1 m. The raster elevation data were spatially matched to the corresponding road segments.

The "*Marktäcke Nedladdning, vektor*" data source provides polygon-based information describing Sweden's physical surface cover. The dataset contains detailed classes representing, among others, agricultural land, forest, built-up land, open land, lakes, watercourses, and wetlands. The product is distributed in GeoPackage format through the STAC download service. Each spatial feature is represented by a polygon geometry and associated categorical attributes identifying the original land-cover type.

The original classification includes more detailed categories than the analysis requires. The source classes were therefore reclassified into four principal environmental groups: forest, open land, urban land, and water. Categories that did not clearly belong to one of these groups were retained as "Other" during the initial processing, as shown in Table 3.1. Figure 3.4 shows the polygon-based structure of

the *Marktäcke Nedladdning, vektor* product.

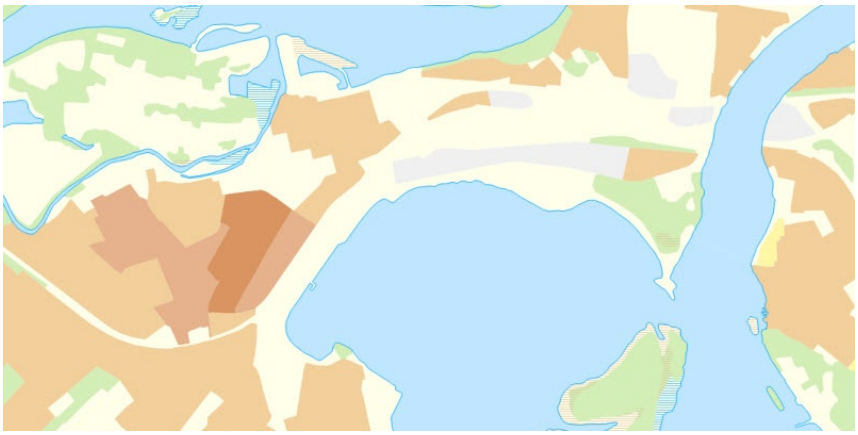


Figure 3.4: Example visualisation of the land-cover polygons provided in *Marktäcke Nedladdning, vektor*. Source: © Lantmäteriet.

The "*Byggnad Nedladdning, vektor*" data source contains polygon geometries representing individual building footprints. It consists of one principal building-area layer, in which each feature may include attributes describing the building type, intended use, collection or geometry type, and, where available, the building name. Building purposes include broad categories such as residential, industrial, and public or community functions. In this study, they were used to support the identification and interpretation of built-up road environments, particularly where local building density and geometric enclosure may affect wind sheltering, wakes, or channeling. Figure 3.5 illustrates the polygon-based structure of the *Byggnad Nedladdning, vektor* dataset.



Figure 3.5: Example visualisation of the building-footprint polygons provided in the *Byggnad Nedladdning, vektor* dataset. Source: © Lantmäteriet.

The data were spatially matched to the road segments and used to calculate the proportions of different land-cover types within a 250 m buffer around each segment

center. These static GIS variables were subsequently used to interpret the spatial wind behavior and shelter-ratio differences described in Section 4.2.2.3.

3.1.4 Route Description

The vehicle measurements were conducted along a transport corridor between the Port of Gothenburg and the Viared logistics area. This route includes a variety of environments such as urban areas, forest sections, and open landscapes, which may influence the local wind field and thermal conditions. The main road where the data is collected is RV (Riksväg) 40.

By combining high-frequency vehicle measurements with regional weather station data, it becomes possible to analyze how local road weather conditions differ from regional meteorological observations and how these differences affect vehicle motion resistance and energy consumption. Figure 3.6 shows the route for a randomly selected trip. The routes for each trip may differ slightly due to circumstances such as roadwork.

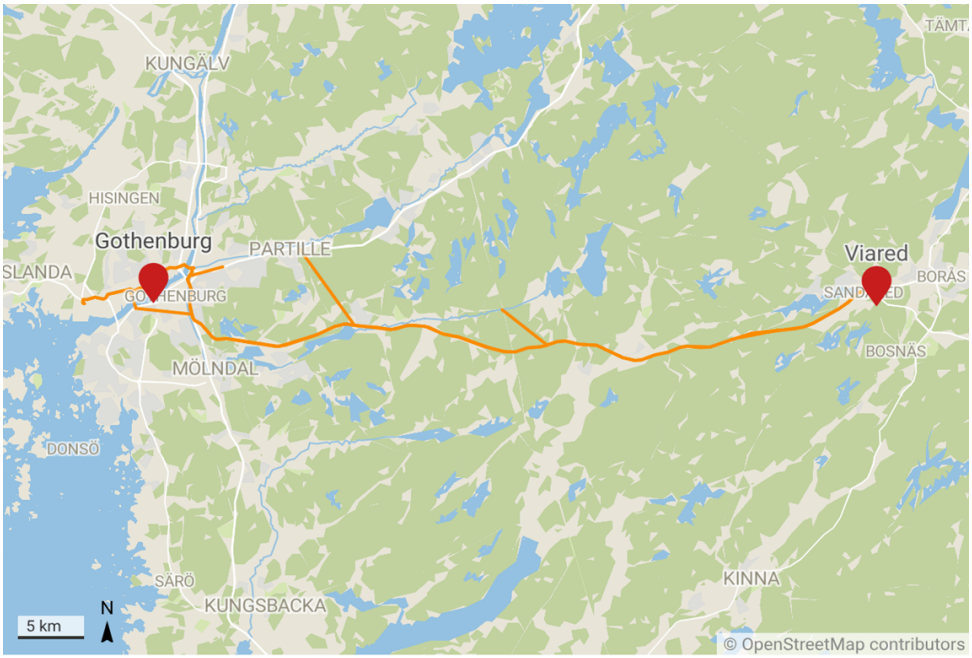


Figure 3.6: Transport route between Gothenburg and Viared used in the vehicle measurement data.

3.2 Absolute Wind Calculation

To calculate the absolute wind speed and direction (v_w, θ), the data from the anemometer (v_{rel}, α) were divided into speed components of headwind and crosswind. The headwind and crosswind components were calculated as:

$$v_{wCross} = v_{rel}\sin(\alpha) \tag{3.1}$$

$$v_{wHead} = v_{rel}\cos(\alpha) - v_v \tag{3.2}$$

The absolute wind speed and direction were calculated as:

$$v_w = \sqrt{v_{wCross}^2 + v_{wHead}^2} \tag{3.3}$$

$$\theta = \arctan2(v_{wCross}, v_{wHead}) + \beta \tag{3.4}$$

Figure 3.7 visualizes the headwind and crosswind components.

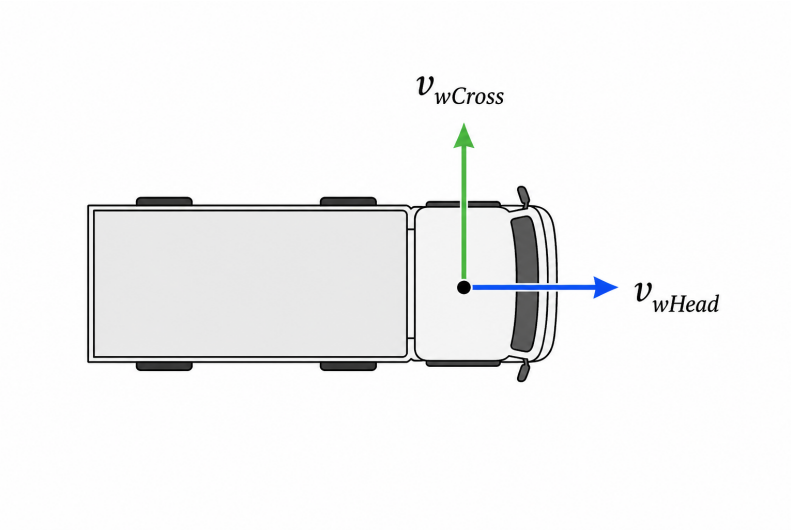


Figure 3.7: Visualization of headwind and crosswind components.

3.3 Wind Sensor Calibration

Vehicle-mounted anemometers are susceptible to several sources of measurement error. The two dominant factors are mechanical misalignment during installation and aerodynamic flow distortion caused by the truck cab geometry. In addition, vehicle steering dynamics and varying environmental conditions can introduce additional measurement noise. Since accurate estimation of aerodynamic drag requires reliable relative wind information, a two-step calibration procedure was implemented to extract the true wind conditions from the raw sensor data. The calibration process consists of (1) wind direction alignment calibration and (2) wind data calibration.

3.3.1 Wind Direction Alignment Calibration

Due to installation errors, the wind sensor may not be perfectly aligned with the vehicle's front-facing axis. As a result, the measured wind direction typically contains a constant angular offset relative to the vehicle reference frame.

Under ideal conditions with negligible ambient wind, the relative wind vector when driving at high speeds should, on average, be coming head-on. The measurements from 200 trips, evenly distributed over a year, were filtered to include only data

when the truck was driving above 19 m/s. A broader set of 200 trips was used for the wind-direction alignment calibration, whereas the subsequent road-segment wind-model analysis was based on 143 valid trips that satisfied the route and signal-quality requirements defined for the modeling dataset. The mean of the respective measured wind angles was then calculated and subtracted from the whole dataset. The method was chosen, because it provides the most statistically robust estimate of the mean wind angle. The mechanically corrected wind direction α is therefore obtained by correcting the raw wind direction measurement α_{raw} according to:

$$\alpha = \alpha_{raw} - \bar{\alpha}_{raw}(v_v > 19 \text{ m/s}) \tag{3.5}$$

3.3.2 Wind Data Calibration

The wind speed recorded in the vehicle CAN data comes from onboard anemometers and may contain systematic errors caused by vehicle motion, sensor installation location, and aerodynamic disturbances around the cab. To reduce the influence of these errors on aerodynamic drag estimation, a wind speed and angle calibration method based on a ground-truth reference was applied.

To record data for the calibration set, a second anemometer was installed at around 1.4 meters above the driver's cab. The truck was driven around an oval test track for two laps at speeds of 50, 60, 70, 80, and 90 km/h. When calibrating the lower anemometer, the goal was to correlate θ and v_w from the lower anemometer with those from the higher anemometer. The truck's wind visor was at the lowest setting for the calibration data, while a high setting was used as validation data for the model. Figure 3.8 shows the truck with the two anemometers installed.



Figure 3.8: Truck used for data collection and calibration.

The data was filtered to include only the straight sections of the track when driving above 45 km/h. For the two straights running in opposite directions, the ambient

wind condition was assumed to be identical. The data was filtered to only contain the straight sections due to large amounts of noise in the turning parts. In practice, local disturbances can cause discrepancies. Using different constant speeds, the analysis of the vehicle's influence will be more general for different speeds.

For the wind angle calibration, the data were separated by vehicle speed and by the straight section of the track on which they were recorded. The windspeed calibration was only based on the deviations between the different absolute windspeeds for the different vehicle speeds. The absolute wind metrics were averaged in these sections to minimize the influence of noise.

The calculated absolute wind speed and direction from the higher anemometer were first calibrated to be independent of vehicle speed and heading, serving as ground truth for calibrating the lower anemometer. The calibration method for both anemometers used only factors and offsets based on the vector itself to adjust the headwind and crosswind components, as well as the calculated absolute wind speed and direction.

3.4 Wind Data Analysis

This section defines the methods for analyzing the wind data.

3.4.1 Road Segmentation

As the raw data contain long vehicle travel paths, the trips were divided into fixed-length segments to enable analysis of specific road sections. This converts continuous vehicle trajectories into discrete spatial analysis units, allowing us to quantify and compare environmental features and factors that affect motion resistance across different road-section types. Here, the trip routes were divided into 500-meter segments. The 500-meter segment length was chosen to balance spatial resolution and representativeness of environmental conditions. Shorter segments might introduce excessive local variability and measurement noise, while longer segments might obscure important changes in environmental factors along the vehicle's route. This segmentation framework lays the foundation for subsequent environmental feature extraction and meteorological data matching.

3.4.2 Wind Angle Sections

One key part of analyzing the wind for different road segments is understanding how regional wind affects local wind. The different trips were divided into 12 groups based on the regional wind direction (SMHI) and then averaged to obtain more statistically reliable data for those sections. The wind speed and direction were then analyzed in 500-meter sections to see whether there were noticeable patterns, such as peaks, dips, or general behaviors that deviated from the average. These findings were then used to select model parameters that predict wind speed and angle across the 500-meter-long sections, based on the direction of the regional background wind

which is defines as the average SMHI wind direction for the section. Figure 3.9 shows how the wind angle sections are divided.

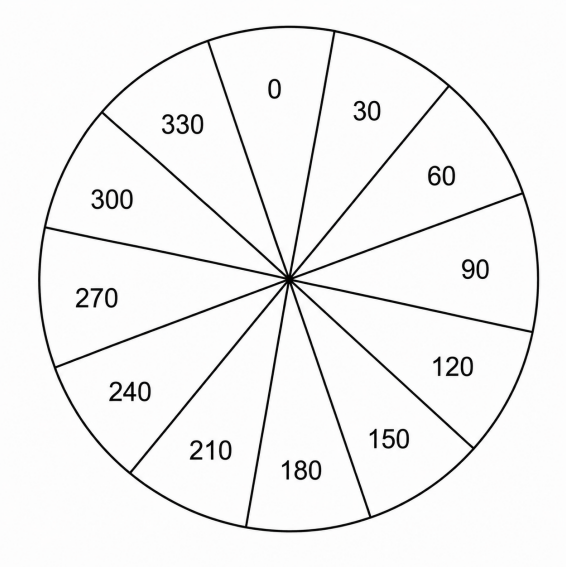


Figure 3.9: Sectioning of wind data.

3.4.3 Topography Analysis

The analysis uses the previously described road segmentation. As stated in the theory chapter, topography can heavily influence the wind. The data were analyzed in relation to the topographical properties of the different road sections. The wind speed and altitude for the different sections were averaged. For each section, a four-edged box in the wind direction was created to act as a topographical area that can affect the wind on the road section. The mean altitude in this area was then compared with the mean altitude of the road section to be used as an important part of the wind prediction model. An example of the area is presented in Figure 3.10.

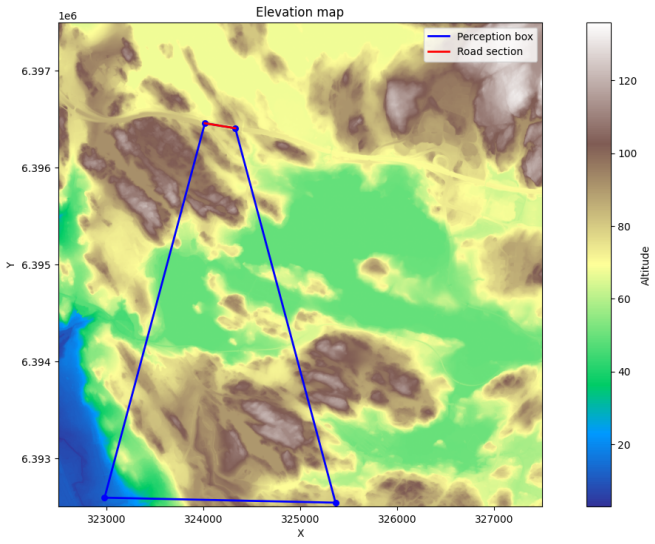


Figure 3.10: Perception box of elevation area.

The goal of the topographical analysis is to create a model $v_w = f(v_{SMHI}, h, H)$ where v_w is the prediction which is determined by a function of the wind velocity from SMHI v_{SMHI}, the average altitude of the road section h and the average altitude of the perception box H.

3.4.4 Landscape Analysis

To estimate the local wind speed at the road-segment level, the calibrated vehicle-mounted anemometer measurements were used as the target, while the SMHI station measurements were used as the regional background wind-speed input.

A hierarchical correction approach was developed because the discrepancy between regional station measurements and road-level wind observations was found to contain systematic effects at different spatial scales. Previous studies have shown that near-surface wind observations are strongly affected by local exposure, surface roughness, vegetation, buildings, and topography, and that regional wind measurements therefore require correction or downscaling when used to represent local wind conditions [23, 24]. Exploratory analysis of the dataset has showed three distinct sources of systematic discrepancy. First, the average relationship between local and SMHI wind speed varied nonlinearly with the regional wind speed, motivating a regional background wind-speed correction. Second, persistent differences remained between groups of road segments with similar wind characteristics, motivating a cluster-level residual correction. Finally, systematic biases remained at individual road segments after the first two corrections, motivating a segment-specific residual correction.

The resulting three-layer model was therefore developed in this thesis as an empirical hierarchical bias-correction framework rather than adopted directly from an

existing three-layer formulation. Layer 1 corrects the regional background wind-speed-dependent bias, Layer 2 applies a cluster-level mean residual correction, and Layer 3 corrects persistent segment-specific residuals.

The complete model is

$$\hat{V}_{\text{final}}(k,i) = \hat{V}_{L1}(k,i) + \Delta_{c(k)} + \mu_{\text{resid}}^{(-i)}(k). \tag{3.6}$$

where $\hat{V}_{L1}(k,i)$ denotes the Layer 1 wind-speed prediction for road segment k during trip i, $\Delta_{c(k)}$ is the Layer 2 residual correction associated with the wind-behavior cluster assigned to segment k, and $\mu_{\text{resid}}^{(-i)}(k)$ is the Layer 3 segment-specific residual correction estimated without using the held-out trip i.

To characterize how the local road-level wind differs from the regional background wind, a dimensionless Shelter Ratio (SR) was introduced. The SR is used as a descriptive measure of the regional-to-local wind relationship, and as one of the statistics used to characterize the wind behavior of individual road segments. Layer 2 uses the mean residual from the Layer 1 prediction within each cluster, as defined below.

For road segment k observed during trip i, the shelter ratio is defined as the ratio between the calibrated local wind speed measured by the vehicle-mounted anemometer and the corresponding regional background wind speed:

$$SR(k,i) = \frac{V_{\text{anem}}(k,i)}{V_{\text{SMHI}}(k,i)}. \tag{3.7}$$

The segment-level mean shelter ratio is computed by averaging over all available trips observing segment k:

$$\overline{SR}_k = \frac{1}{N_k} \sum_{i=1}^{N_k} SR(k,i), \tag{3.8}$$

where N_k is the number of valid trip observations for segment k. Here, a "valid trip" is defined as a journey whose vehicle trajectory follows the predefined primary study route, RV40, and for which the required vehicle and meteorological signals are continuously available for a sufficiently long duration. Observations containing missing or invalid vehicle or weather data are excluded from the analysis.

Here, the shelter ratio provides a dimensionless measure of the relative difference between the road-level wind and the regional background wind. A value of $SR(k,i) = 1$ indicates that the locally measured wind speed is equal to the corresponding SMHI background wind speed. Values below unity, $SR(k,i) < 1$, indicate that the local road-level wind is attenuated relative to the regional background, whereas values above unity, $SR(k,i) > 1$, indicate that the local wind is stronger than the regional reference. The ratio therefore provides a direct way of distinguishing locally

sheltered and locally wind-amplified conditions independently of the absolute wind-speed magnitude.

The segment-level mean $\overline{SR}_k$ summarizes whether a road segment systematically tends to experience weaker or stronger wind than the regional background across repeated trips. Values persistently below or above unity can therefore indicate a recurring local effect associated with the road environment, while values close to unity indicate that the regional wind measurement is more representative of the local road-level condition.

Although the Shelter Ratio is useful for characterizing the regional-to-local wind relationship and for describing segment-level wind behavior, it is not directly used as the Layer 2 correction term. Instead, Layer 2 is based on the residual remaining after the Layer 1 global correction.

The Layer 1 residual for road segment k during trip i is defined as

$$r_{L1}(k,i) = V_{\text{anem}}(k,i) - \hat{V}_{L1}(k,i). \tag{3.9}$$

After assigning road segments to clusters, the Layer 2 correction for cluster c is defined as the mean Layer 1 residual over all valid segment–trip observations belonging to that cluster:

$$\Delta_c = \frac{1}{N_c} \sum_{(k,i)\in c} r_{L1}(k,i), \tag{3.10}$$

where N_c denotes the total number of valid segment–trip observations assigned to cluster c. The cluster-level residual Δ_c therefore represents the average systematic Layer 1 prediction bias shared by road segments with similar wind behavior. The Layer 2 prediction is obtained by adding this correction to the Layer 1 prediction.

The following subsections describe the formulation and role of each model layer in detail, including the clustering procedure used to derive these segment groups.

3.4.4.1 Layer 1: Global Correction

The trip-level data showed a systematic dependence of the mean shelter ratio on the SMHI background wind speed. As shown in Figure 3.11, the shelter ratio generally decreased with increasing SMHI wind speed and was not approximately constant over the observed range. This indicates that a constant scaling factor would not adequately represent the regional-to-local wind relationship. The observed relationship also exhibited a curved trend, motivating the use of a simple nonlinear formulation rather than assuming a linear dependence.

A power-law function was therefore adopted as a parsimonious empirical representation of the observed relationship. The power law requires only two parameters, preserves a positive and monotonic mapping for positive wind speeds, and follows

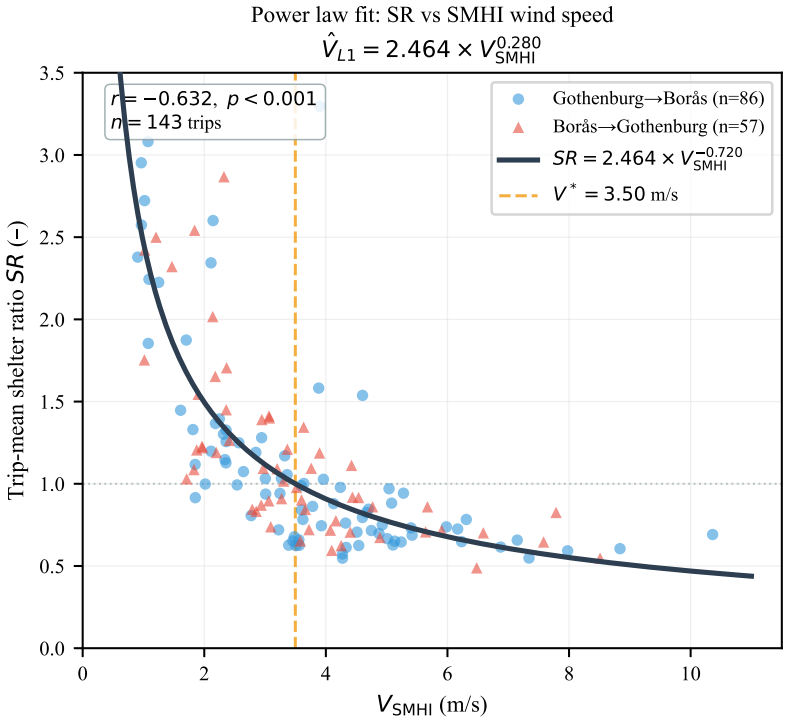


Figure 3.11: Relationship between trip-mean shelter ratio SR_i and SMHI background wind speed $V_{\mathrm{SMHI},i}$ for the 143 analyzed trips. The solid curve represents the fitted power-law relationship used for the Layer 1 global correction.

the curvature observed in the trip-level data. The model form was selected based on the observed data pattern rather than through a systematic comparison of alternative linear and nonlinear formulations. Consequently, other functional forms may provide comparable or improved performance, which remains a limitation of the present model-selection procedure.

$$\hat{V}_{L1}(k,i) = a\, V_{\mathrm{SMHI}}(k,i)^{1+b}, \tag{3.11}$$

The coefficients a and b were estimated from trip-level aggregated data. For each trip i, the shelter ratios of all valid segment observations were averaged to obtain the trip-mean shelter ratio $\overline{SR}_i$. The corresponding SMHI background wind speeds were likewise aggregated over the valid observations within the trip to obtain a representative trip-level wind speed $\overline{V}_{\mathrm{SMHI},i}$. The power-law relationship was fitted to the 143 trip-level pairs $(\overline{V}_{\mathrm{SMHI},i}, \overline{SR}_i)$.

In this formulation, a defines the overall scale of the regional-to-local correction, while the exponent b describes how the relative local wind response changes with the magnitude of the regional background wind. If $b = 0$, the shelter ratio is constant and the regional-to-local relationship reduces to a simple multiplicative scaling. A negative value of b indicates that the relative local wind speed decreases as the regional background wind becomes stronger, whereas a positive value indicates an increasing relative local response with increasing background wind speed.

After fitting the coefficients, the resulting power law was applied at the segment–trip level. Thus, for road segment k during trip i, $V_{\mathrm{SMHI}}(k,i)$ denotes the regional background wind speed matched to that particular observation, and $\hat{V}_{L1}(k,i)$ denotes the corresponding Layer 1 local wind-speed prediction.

Overall, the shelter-ratio formulation and the fitted power-law relationship allow Layer 1 to transform the regional SMHI wind speed into a first-order estimate of local road-level wind by accounting for the systematic dependence of the regional-to-local wind ratio on background wind speed. This captures the regional background wind-behavior observed across trips, but not persistent location-specific deviations between road segments, which are addressed in Layer 2.

3.4.4.2 Layer 2: Wind-behavior Cluster Correction

Although Layer 1 captures the regional background wind-speed-dependent relationship between regional and local wind, persistent spatial differences remain between individual road segments. Such differences may be associated with local environmental conditions, including vegetation, built-up areas, open terrain, and other site-specific exposure characteristics.

To account for these persistent spatial differences, road segments are grouped according to their observed wind behavior, and a cluster-level correction is subsequently applied to each group.

For each segment, wind behavior statistics are computed by aggregating observations across all available trips. These aggregated statistics form the input feature vector used for K-means clustering. Aggregating the observations across repeated trips reduces the influence of trip-specific meteorological variability and allows the feature vector to emphasize the persistent wind-behavior characteristics of each road segment.

K-means clustering is an unsupervised learning method that partitions observations into a predefined number of groups by minimizing the within-cluster distance between each observation and its assigned cluster centroid. In this study, each observation provided to K-means represents one road segment described by its aggregated wind-behavior features. The purpose of the clustering is therefore to identify groups of road segments that exhibit similar persistent regional-to-local wind behavior, without imposing predefined environmental labels.

For each eligible road segment k, the observations collected across repeated trips were aggregated into a wind-behavior feature vector,

$$\mathbf{x}_k = \left[\overline{SR}_k,\ \sigma_{SR,k},\ CV_{SR,k},\ IQR_{SR,k},\ \overline{\Delta V}_k,\ \overline{\Delta\theta}_k\right], \tag{3.12}$$

where $\overline{SR}_k$ is the mean shelter ratio of segment k across repeated trips, $\sigma_{SR,k}$ is the corresponding standard deviation, $CV_{SR,k}$ is the coefficient of variation, and $IQR_{SR,k}$ is the interquartile range of the shelter ratio. The term $\overline{\Delta V}_k$ denotes

the mean difference between the local road-level wind speed and the corresponding SMHI background wind speed, while $\overline{\Delta\theta}_k$ denotes the mean difference between the local and SMHI wind directions.

These features were selected to characterize both the average regional-to-local wind relationship and its variability across repeated trips. The shelter-ratio statistics describe the typical magnitude and consistency of local wind attenuation or amplification, while the wind-speed and wind-direction deviations capture systematic differences between the local road-level wind and the regional background condition.

Before applying K-means clustering, the clustering features were normalized using min–max scaling. Each feature was scaled independently to the interval $[0, 1]$ according to

$$x' = \frac{x - x_{\min}}{x_{\max} - x_{\min}}, \tag{3.13}$$

where x denotes the original feature value, and $x_{\min}$ and $x_{\max}$ denote the minimum and maximum values of that feature in the clustering dataset. This scaling places variables with different numerical ranges on a comparable basis and prevents features with larger magnitudes, particularly wind-direction and wind-speed deviations, from dominating the Euclidean distance used by K-means.

The clustering is based exclusively on the wind-behavior statistics and does not directly use geographic variables as clustering features. Geographic land-cover data from Lantmäteriet, including forest, urban, open-land, and water fractions within a 250 m buffer around each road segment, are instead used after clustering to interpret the physical and environmental characteristics associated with each cluster. The original Lantmäteriet land-cover classes were therefore mapped to the broader environmental categories shown in Table 3.1.

Only road segments observed in at least 50 valid trips were included in the K-means clustering. This threshold was used to ensure that the segment-level wind-behavior features were estimated from a sufficient number of repeated observations. The normalized feature vectors defined above were then used for K-means clustering.

The Layer 2 prediction is obtained by adding the mean Layer 1 residual of the assigned cluster:

$$\hat{V}_{L2}(k, i) = \hat{V}_{L1}(k, i) + \Delta_{c(k)}. \tag{3.14}$$

where $c(k)$ denotes the cluster assigned to road segment k, and $\Delta_{c(k)}$ denotes the mean Layer 1 residual over all valid segment–trip observations belonging to that cluster.

$$\Delta_c = \frac{1}{N_c} \sum_{(k,i)\in c} \left(V_{\text{anem}}(k, i) - \hat{V}_{L1}(k, i) \right). \tag{3.15}$$

Table 3.1: Mapping from Lantmäteriet Marktäcke categories to the four land cover classes used in this study. Data from Byggnad Nedladdning and Marktäcke Nedladdning, vektor.

Original type	**Description**	**Class**
Barrskog och blandskog	Coniferous and mixed forest	Forest
Lövskog	Deciduous forest	Forest
Sjö	Lake	Water
Hav	Sea	Water
Vattendragsyta	Watercourse surface	Water
Anlagt vatten	Artificial water body	Water
Öppen mark	Open land	Open
Åker	Arable land	Open
Låg bebyggelse	Low-rise development	Urban
Industri- och handelsbebyggelse	Industrial and commercial	Urban
Torg	Public square	Urban
Hög bebyggelse	High-rise development	Urban
Sluten bebyggelse	Dense urban development	Urban
All others	*Unclassified*	*Other*

where N_c is the total number of valid segment–trip observations belonging to cluster c.

Overall, Layer 2 captures systematic residual differences shared by groups of road segments with similar long-term wind behavior. These group-level differences may reflect recurring local exposure and environmental effects that are not represented by the global Layer 1 correction.

3.4.4.3 Layer 3: Segment Residual Correction

After the first two layers, individual segments may retain a systematic bias because location-specific wind effects cannot be resolved by the cluster-level correction. Examples include acceleration through narrow gaps in forest cover, channeling by buildings, or exposure to open water. Layer 3 estimates a fixed residual correction for each segment from its historical observations.

The residual after Layer 2 for segment k on trip i is defined as

$$\varepsilon(k,i) = V_{\text{anem}}(k,i) - \hat{V}_{L2}(k,i) \tag{3.16}$$

and the mean residual across all available trips is

$$\mu_{\text{resid}}(k) = \frac{1}{N_k} \sum_{i=1}^{N_k} \epsilon(k, i). \tag{3.17}$$

If this mean residual is applied directly to evaluate predictions on the same trips used to compute it, the residual correction would absorb trip-specific noise and inflate the apparent model performance. To prevent this, the correction applied to held-out trip i is computed from the remaining trips only:

$$\mu_{\text{resid}}^{(-i)}(k) = \frac{1}{N_k - 1} \sum_{\substack{j=1 \\ j \neq i}}^{N_k} \epsilon(k, j) \tag{3.18}$$

where N_k denotes the number of valid trip observations available for road segment k. For the prediction of trip i, the residual correction is calculated using all valid observations of segment k except the held-out trip.

The final prediction is then

$$\hat{V}_{\text{final}}(k, i) = \hat{V}_{L1}(k, i) + \Delta_{c(k)} + \mu_{\text{resid}}^{(-i)}(k). \tag{3.19}$$

Overall, Layer 3 improves the prediction by adding the historical mean residual of each road segment to the Layer 2 estimate. This allows persistent segment-specific biases to be compensated for when the same segment is encountered again. However, because the correction depends directly on residuals previously observed for that specific segment, its applicability is limited to road segments represented in the training data. Layer 3 should therefore be regarded as a route-specific refinement rather than a transferable correction for unseen roads or regions.

3.4.4.4 Model Evaluation

All model layers were evaluated using leave-one-out cross-validation (LOO-CV) at the trip level. In each iteration, one of the 143 valid trips was held out in its entirety and treated as an unseen journey, while the model was fitted using the remaining 142 trips. The fitted model was then applied to all valid road-segment observations in the held-out trip.

For a given held-out trip i, the corresponding SMHI background wind speed $V_{\text{SMHI}}(k, i)$ was used as the model input for each road segment k. The Layer 1, Layer 2, and Layer 3 predictions were then generated for that segment, with the Layer 3 residual correction calculated without using any observation from the held-out trip. The predicted local wind speed was compared with the calibrated anemometer measurement $V_{\text{anem}}(k, i)$ to obtain the prediction error for each segment. After all segments in the held-out trip had been evaluated, the same procedure was repeated with each of the remaining trips serving once as the held-out trip. Consequently, every trip was evaluated using a model that did not use that trip for its prediction.

The prediction errors from all 143 held-out trips were subsequently combined to calculate the overall mean absolute error (MAE). The same held-out observations were used to evaluate the SMHI baseline and each successive correction layer, allowing the incremental contribution of Layer 1, Layer 2, and Layer 3 to be compared on a consistent basis.

The trip, rather than the individual road-segment observation, was used as the cross-validation unit because observations collected within the same trip are not statistically independent: they share the same large-scale meteorological conditions, measurement setup, and temporal context. Randomly separating segment-level observations from the same trip between the training and evaluation sets could therefore lead to information leakage and an overly optimistic estimate of predictive performance. Grouped or blocked cross-validation is generally recommended when observations contain hierarchical, temporal, or other dependence structures [25]. Holding out complete trips was therefore chosen to evaluate how well the model generalizes to an unseen journey with its own combination of meteorological conditions and measurement sequence.

Model performance was quantified using the mean absolute error (MAE) between the predicted road-level wind speed and the calibrated anemometer measurements over all held-out segment–trip observations. MAE was selected because it expresses the average prediction error directly in wind-speed units (m/s), providing an intuitive measure of prediction accuracy and facilitating comparison with the SMHI baseline. The MAE obtained after each correction layer was compared with the baseline MAE to quantify the incremental improvement introduced by the model.

In addition to the overall LOO-CV performance, the prediction errors were examined across different SMHI background wind-speed ranges. This stratification was used to determine whether the correction remained effective across the observed wind-speed range, rather than achieving a low overall error primarily because most observations occurred under a limited set of wind conditions. This analysis is particularly relevant because the Layer 1 correction was motivated by a wind-speed-dependent bias in the regional-to-local wind relationship.

Finally, the LOO-CV results were grouped by month to examine whether model performance was consistent across different periods of the year. Monthly comparisons provide an indirect assessment of robustness to changing seasonal and meteorological conditions, since the distribution of wind speed, wind direction, and trip frequency varies over the annual measurement period. The monthly analysis was not intended as an independent seasonal validation, but rather as a diagnostic check of whether the observed improvement was concentrated in a limited subset of the data.

Together, these evaluations were designed to assess three complementary aspects of model performance: generalization to unseen trips, robustness across different regional wind-speed conditions, and consistency over the annual measurement period.

3.4.5 Wind Direction Model

The wind direction model was formulated with a polynomial to capture the general trend in a highly noisy variable such as wind direction. Channeling effects were represented using a polynomial regression that maps the regional wind angle obtained from SMHI to the corresponding measured mean wind angle. The measured mean wind angles were computed from the dataset by gathering observations by regional wind angle, following the wind angle section method. This regression therefore provides a transfer function from regional to site-influenced wind direction based on the road heading, while avoiding overfitting to short-term fluctuations.

3.5 Rolling Resistance Modeling

As mentioned earlier, rolling resistance represents one of the major energy losses for vehicles, particularly under winter operating conditions. Tire properties, road surface characteristics, and thermal conditions strongly influence it. Therefore, accurately estimating rolling resistance requires a reliable representation of the tire thermal state.

In this study, rolling resistance is modeled using longitudinal vehicle dynamics and a tire temperature estimation framework. A two–state tire temperature observer is used to capture the thermal dynamics between the tire and the road surface.

3.5.1 Two-State Tire Temperature Observer

The two states represent the internal thermal energy stored in the tire rubber and the air inside the tire cavity. The state vector is defined as:

$$x = \begin{bmatrix} T_{TB} \\ T_{TA} \end{bmatrix} \tag{3.20}$$

where T_{TB} denotes the tire bulk average temperature and T_{TA} denotes the cavity air temperature. Figure 3.12 illustrates where the different temperatures are taken.

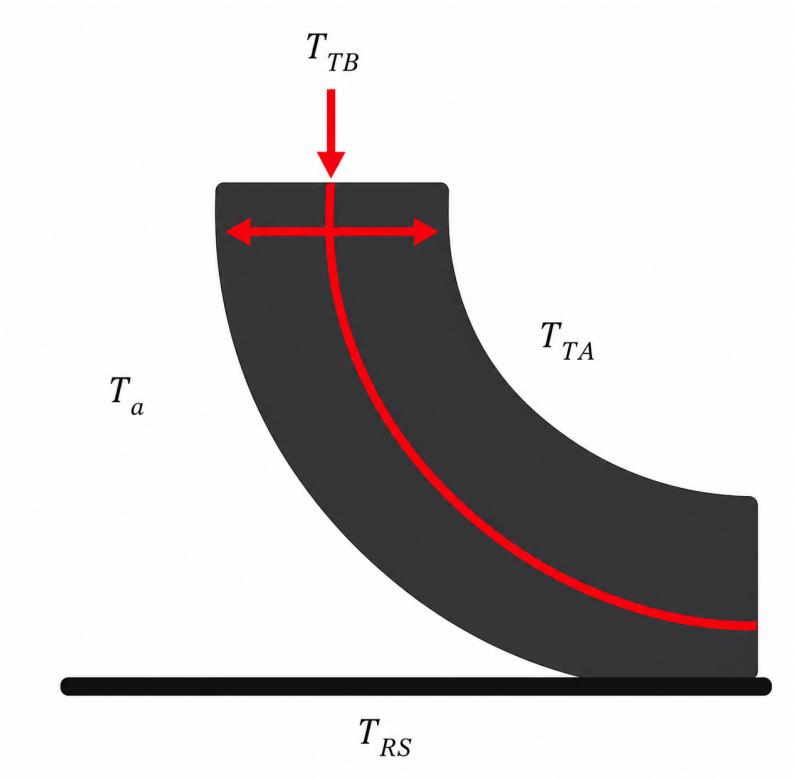


Figure 3.12: Visualization of temperatures.

The tire thermal dynamics are modeled as a linear parameter-varying (LPV) state-space system

$$\dot{x} = A(v_v, c_{RS})x + Bu + F(v_v, c_{RS})d \tag{3.21}$$

where v_v represents the vehicle speed and c_{RS} denotes the road surface condition index. A and F are 2x2 matrices, while B is a 2x1 vector. The system input corresponds to the rolling resistance power dissipated as heat

$$u = P_{rr} \tag{3.22}$$

where P_{rr} represents the hysteresis losses generated in the tire due to cyclic rubber deformation during rolling. The disturbance vector is defined as

$$d = \begin{bmatrix} T_{RS} \\ T_a \end{bmatrix} \tag{3.23}$$

where T_{RS} denotes the road surface temperature and T_a the ambient air temperature.

The temperature dynamics of the two-state model are governed by the system matrix

$$A(v_v, c_{RS}) = \begin{bmatrix} -\frac{c_{11}+c_{2x}(c_{RS},v_v)+c_{34}}{m_{t2}c_{t2}} & \frac{c_{34}}{m_{t2}c_{t2}} \\ \frac{c_{34}}{m_{ta}c_{ta}} & -\frac{c_{34}+c_{61}}{m_{ta}c_{ta}} \end{bmatrix} \tag{3.24}$$

The input matrix is defined as

$$B = \begin{bmatrix} \frac{1}{m_{t2}c_{t2}} \\ 0 \end{bmatrix} \tag{3.25}$$

and the disturbance distribution matrix

$$F(v_v, c_{RS}) = \begin{bmatrix} \frac{c_{11}}{m_{t2}c_{t2}} & \frac{c_{2x}(c_{RS},v_v)}{m_{t2}c_{t2}} \\ 0 & \frac{c_{34}+c_{61}}{m_{ta}c_{ta}} \end{bmatrix} \tag{3.26}$$

The model output corresponds to the cavity air temperature measured by the tire pressure monitoring system (TPMS)

$$y = Cx \tag{3.27}$$

with

$$C = \begin{bmatrix} 0 & 1 \end{bmatrix} \tag{3.28}$$

The model is shown in a block diagram in Figure 3.13.

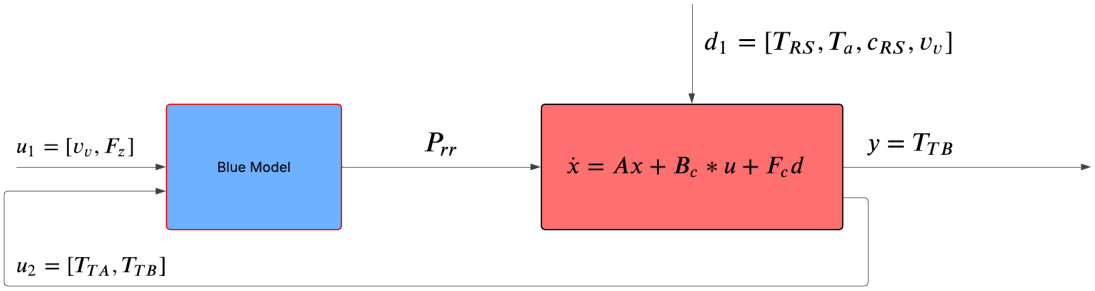


Figure 3.13: Block diagram of tire temperature model.

For the internal tire bulk temperature to be reconstructed through the observer dynamics, the systems must be observable. The system is observable if the observability matrix $\mathcal{O}$ has full rank.

$$\mathcal{O} = \begin{bmatrix} C \\ CA \end{bmatrix} \tag{3.29}$$

Since the A-matrix has a non-zero second row, the system will be observable.

The cavity air temperature was calculated by using the tire pressure and the ideal gas law, assuming constant volume.

$$T_{TA} = \frac{p_T V}{NR} \tag{3.30}$$

This estimated tire bulk temperature is subsequently used to determine the rolling resistance coefficient and capture the influence of ambient temperature, road surface temperature, and driving conditions on tire hysteresis losses. The meteorological influence on rolling resistance can be represented conceptually as

$$C_{rr} = f(T_T, T_{RS}, T_{air}, C_R S, v_v), \tag{3.31}$$

where T_T represents the dynamic tire temperature, T_{RS} and T_{air} represent the road-surface and ambient air temperatures, C_RS represents the road-surface condition, and v_v is the vehicle speed. This formulation allows the rolling resistance to vary according to both the thermal state of the tire and the prevailing environmental conditions.

To improve the bulk temperature state estimate, a Kalman filter was used to incorporate our cavity temperature measurements. The corresponding equations for the Kalman filter are eq. 3.32-3.37.

$$\hat{x}[k] = A[k-1]x[k-1] + B[k-1]u[k-1] \tag{3.32}$$
$$\hat{P}[k] = A[k-1]P[k-1]A^T[k-1] + Q \tag{3.33}$$
$$\hat{y}[k] = C\hat{x}[k] \tag{3.34}$$
$$K = \hat{P}[k]C^T(C\hat{P}[k]C^T + R)^{-1} \tag{3.35}$$
$$x[k] = \hat{x}[k] + K(y - \hat{y}[k]) \tag{3.36}$$
$$P[k] = (I - KC)\hat{P}[k] \tag{3.37}$$

The model with the Kalman filter is shown in a block diagram in Figure 3.14.

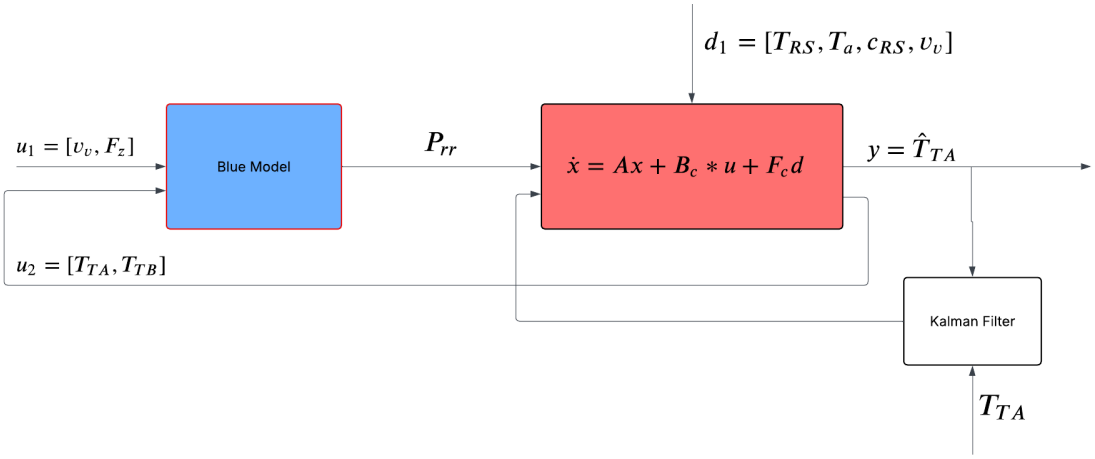


Figure 3.14: Block diagram of model with Kalman filter.

4

Results

This chapter presents the results from the methods described in the previous chapter. The findings are discussed in relation to the thesis's overall aim. Where relevant, the results are compared across measurement setups and across driving environments to highlight systematic patterns, uncertainties, and situations where local on-road wind deviates from regional wind.

4.1 Wind Data Calibration

The results from calibrating the wind data are presented.

4.1.1 Alignment Error

When driving at speeds above 19 m/s, the resulting mean offset for the lower anemometer was calculated to -0.474 degrees. The mean offset for the higher anemometer was calculated to -0.868 degrees. These values was first subtracted from the wind angle data before any other calibration. The measurements from the high anemometers are to be perceived as the ground truth since the measurements are recorded at a height where the vehicle induced disturbances are insignificant.

4.1.2 Data Calibration

The wind calibration results for the low anemometer are:

$$v_{wCross} = 1.276 V_w \sin(\alpha) \tag{4.1}$$

$$v_{wHead} = 0.927(v_{rel}\cos(\alpha) - v_v) \tag{4.2}$$

$$v_w = \sqrt{v_{wCross}^2 + v_{wHead}^2} \tag{4.3}$$

$$\theta = \arctan2(v_{wCross}, v_{wHead}) + \beta \tag{4.4}$$

The results of the calibration are presented in Figure 4.1, which compares the measurements for the different anemometers before and after calibration (observe that $V_h = \beta$ and v_v have been altered to increase graph quality; $W_{dir} = \theta$). The x-axis in the wind angle plot shows the average absolute wind angle for each straight section in the oval track.

It is observable that the wind angle noise decreases, and the wind speed is corrected towards the ground truth. The plot also shows SMHI wind speed and direction, highlighting the difference between regional and local weather.

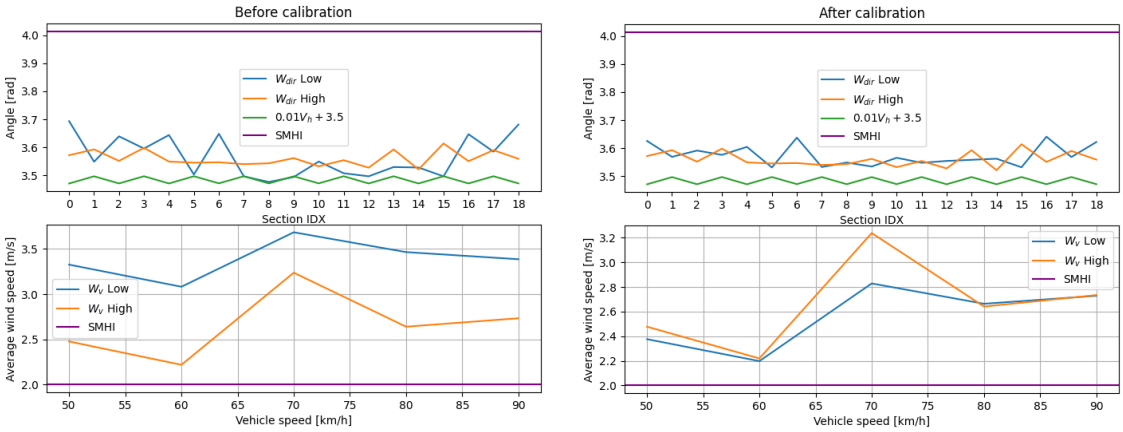


Figure 4.1: Results of calibration for the average of all trips.

The calibration method was validated by comparison with measurements taken at a higher wind visor setting. The wind visor is installed further back than the low anemometer and should not affect the measurements. Figure 4.2 shows the same graph.

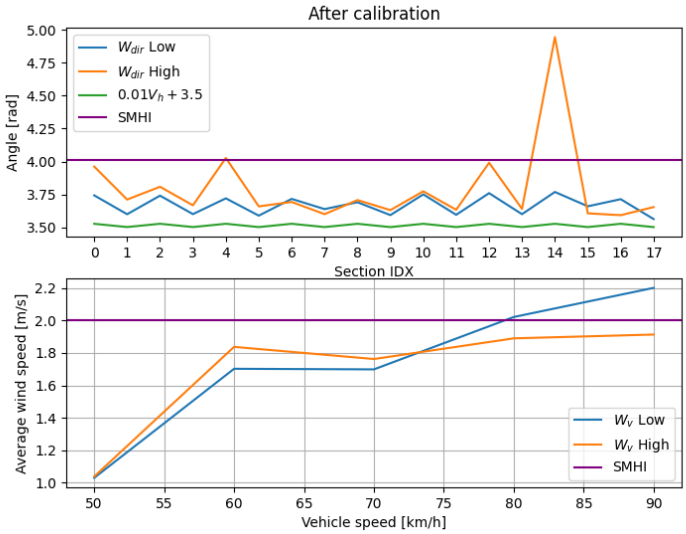


Figure 4.2: Results of calibration with high wind visor setting.

It is visible in Figure 4.2 when comparing the shape of the vehicle heading V_h and mainly W_dir low that there is a slight correlation. It is possible that the cab roof still affects the anemometer by changing the flow profile, but the most probable cause is that the data calibration will not be universal for all trips. Since the wind

direction is a very noisy signal, the final output of the calibration would only be to minimize the correlation with the heading and other factors.

4.2 Wind Models

The different models for predicting local wind behavior are presented.

4.2.1 Topographic Model

The perception box was set to 3000 m to provide a sufficiently large representation of the surrounding terrain while limiting unnecessary computational complexity. Given the absence of high mountains in the vicinity of the road, terrain located beyond this distance is not expected to substantially affect the local conditions represented by the model. At the same time, the 3000 m extent is sufficiently large to capture potentially large open areas surrounding the road. A systematic sensitivity analysis of the perception-box size was not conducted and is therefore not presented here. Consequently, 3000 m should be regarded as a modeling choice rather than a demonstrated RMSE-optimal value. A larger box is unnecessary since there are no high mountains around the road. The box is also large enough to accommodate a potentially large open area.

The model was determined as:

$$v_w = v_{SMHI} + 0.03(\bar{h} - \bar{H}) \tag{4.5}$$

where $\bar{h}$ is the average altitude of the road section and $\bar{H}$ is the average altitude of the perception box. The coefficient (0.03) should be investigated further and adjusted to account for different altitude differences, as it is unlikely to be universally applicable.

4.2.2 Landscape Wind Model

The results from the landscape model are presented and discussed.

4.2.2.1 Three-Layer Wind Speed Correction Model

All model layers were evaluated using leave-one-out cross-validation (LOO-CV) at the trip level, whereby each of the 143 trips was held out in its entirety, and the model was trained on the remaining 142 trips. This procedure ensures that reported performance metrics reflect generalization to unseen trips and prevents data leakage between training and evaluation. Figure 4.3 and Table 4.1 summarize the progressive improvement across layers.

Figure 4.4 shows the three-layer model applied to one randomly selected trip from the 143 valid trips. The example is included only to illustrate the along-route behavior of the measured, baseline, and corrected wind-speed profiles.

Table 4.1: LOO-CV mean absolute error (MAE) for each model layer.

Model	MAE (m/s)	Improvement vs. SMHI
SMHI baseline	1.778	—
Layer 1	1.223	31.2%
Layer 1+2	1.081	39.2%
Layer 1+2+3	1.020	42.6%

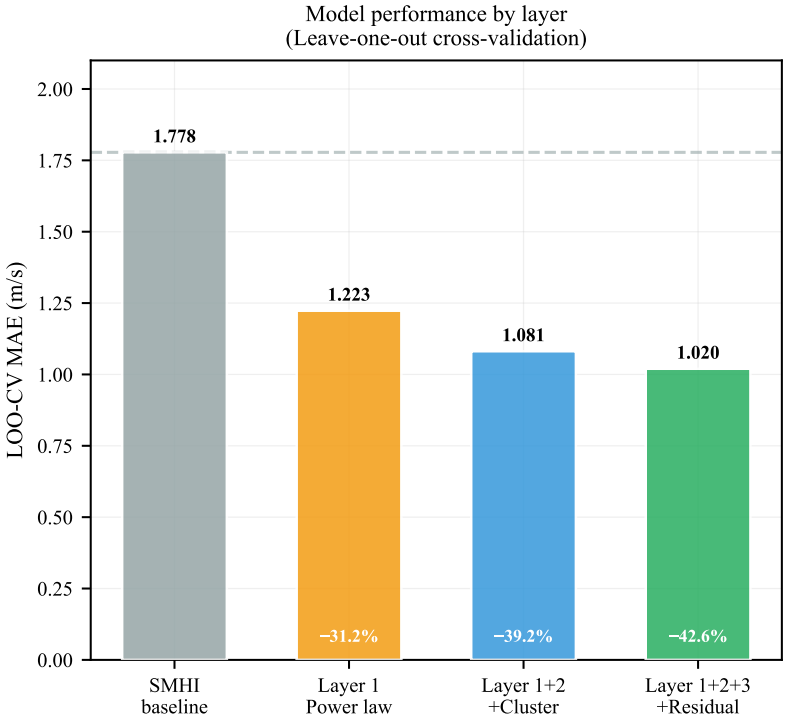


Figure 4.3: LOO-CV MAE for each model layer.

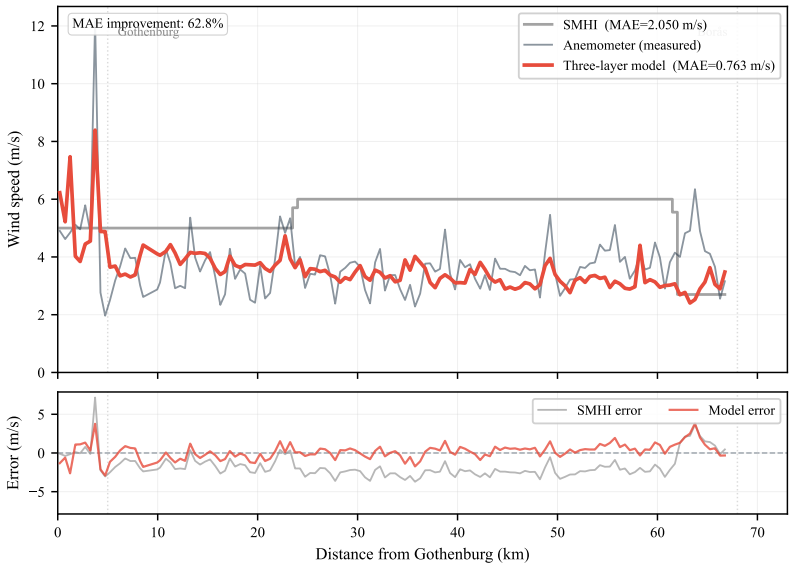


Figure 4.4: Prediction for one randomly selected trip from the 143 valid trips. Upper panel: SMHI background wind speed, measured anemometer wind speed, and three-layer model prediction along the RV 40 route. Lower panel: prediction error for the SMHI baseline and the three-layer model.

4.2.2.2 Layer 1: Global Correction

Trip-level analysis revealed a strong negative correlation between the trip-mean shelter ratio $\overline{SR}_i$ and the SMHI background wind speed $V_{\mathrm{SMHI},i}$ ($r = -0.632$, $p < 0.001$; Figure 3.11). This indicates a systematic wind-speed-dependent difference between the regional SMHI measurements and the road-level wind observations. At lower SMHI wind speeds, the road-level measurements were on average higher than the regional reference, resulting in $\overline{SR}_i > 1$, whereas at higher SMHI wind speeds the opposite tendency was observed, with $\overline{SR}_i < 1$.

The observed relationship may reflect differences in local exposure between the meteorological station and the road environment, including sheltering, surface roughness, and other site-specific effects. However, the present dataset does not allow these mechanisms to be isolated individually. The relationship is therefore treated empirically through the Layer 1 correction.

A power law was fitted to the trip-level $(V_{\mathrm{SMHI},i}, \overline{SR}_i)$ pairs:

$$f(V_{\mathrm{SMHI}}) = 2.464 \times V_{\mathrm{SMHI}}^{-0.720} \tag{4.6}$$

yielding the Layer 1 wind speed prediction:

$$\hat{V}_{L1}(k,i) = V_{\mathrm{SMHI}}(k,i)\left[2.464\, V_{\mathrm{SMHI}}(k,i)^{-0.720}\right] = 2.464\, V_{\mathrm{SMHI}}(k,i)^{0.280}. \tag{4.7}$$

The crossover point $V^* = 3.498$ m/s corresponds to the wind speed at which the

fitted regional-to-local correction factor equals one. Below this value, the fitted correction factor is greater than one, whereas above it the fitted correction factor is less than one.

4.2.2.3 Layer 2: Wind-Behavior Cluster Correction

After Layer 1, systematic residuals remained across road segments, indicating that the global power-law correction did not fully capture persistent spatial differences in wind behavior. Only road segments observed in at least 50 valid trips were included in the clustering analysis, so that the segment-level statistics were based on a sufficient number of repeated observations. This criterion resulted in 172 eligible road segments, each supported by at least 50 repeated trip observations.

For each eligible road segment, wind-behavior statistics were calculated across repeated trips, including the mean and variability of the shelter ratio, the mean wind-speed deviation from the SMHI value, and the mean wind-direction deviation. These statistics were used as the input features for K-means clustering.

The number of clusters was selected by comparing silhouette scores for a small set of candidate solutions, $k \in \{2, 3, 4, 5\}$. The two-cluster solution produced the highest silhouette score, 0.330, and was therefore selected for the subsequent analysis.

The two clusters exhibit clearly distinct wind-behavior characteristics and are associated with different geographic compositions (Figure 4.5 and Figure 4.6). For each cluster, the Layer 1 residuals from all valid segment–trip observations associated with the road segments assigned to that cluster were pooled, and their mean was used as the cluster-level correction Δ_c.

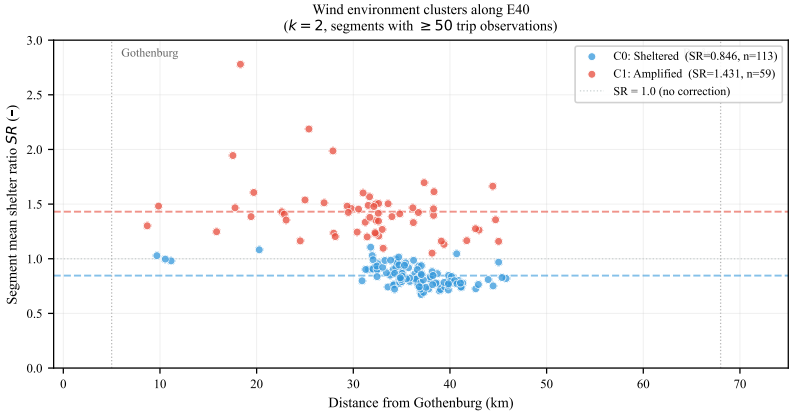


Figure 4.5: Spatial distribution of wind-behavior clusters along RV 40.

- **C0 — Sheltered** ($n = 113$ segments): mean $SR = 0.846$, predominantly located in the forested mid-section of Road (10–46 km from Gothenburg), with a mean forest cover fraction of 0.726 and a mean urban cover fraction of 0.072. The negative deviation from the global correction ($\Delta = -0.833$ m/s) is consistent with the predominantly forested composition of this cluster, where mechanical sheltering may reduce local wind speed relative to the regional background.

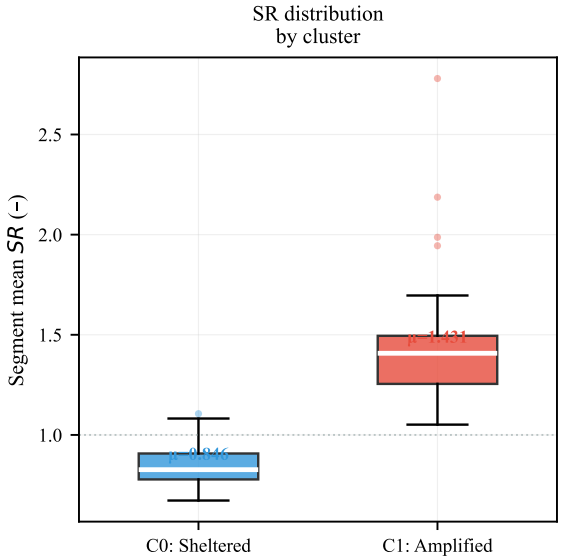


Figure 4.6: Distribution of segment-mean shelter ratio SR by cluster.

- **C1 — Amplified** ($n = 59$ segments): mean $SR = 1.431$, concentrated near the urban endpoints of the route (Gothenburg and Borås), with a mean urban cover fraction of 0.287 and lower forest cover (0.384). The positive deviation ($\Delta = +0.303$ m/s) is consistent with the greater urban exposure of this cluster, where building-induced channeling and local flow acceleration may increase the measured local wind speed relative to the regional background.

These cluster-level additive corrections were applied on top of the Layer 1 prediction:

$$\hat{V}_{L2}(k, i) = \hat{V}_{L1}(k, i) + \Delta_{c(k)} \tag{4.8}$$

where $c(k) \in \{0, 1\}$ denotes the cluster assignment of segment k and Δ_c is the cluster-level mean residual from Layer 1. Segments without a cluster assignment (those visited by fewer than 50 trips, primarily in the urban approach sections) retained the Layer 1 prediction.

The spatial distribution of the two wind-behavior clusters is shown in Figure 4.5, while Figure 4.6 shows the distribution of segment-mean shelter ratio within each cluster. The general land-cover composition along the study route is presented separately in Figure 4.7 and Table 4.2.

Layer 2 reduced the LOO-CV MAE from 1.223 m/s to 1.081 m/s, an additional 8.0 percentage points of improvement over the SMHI baseline (total: 39.2%).

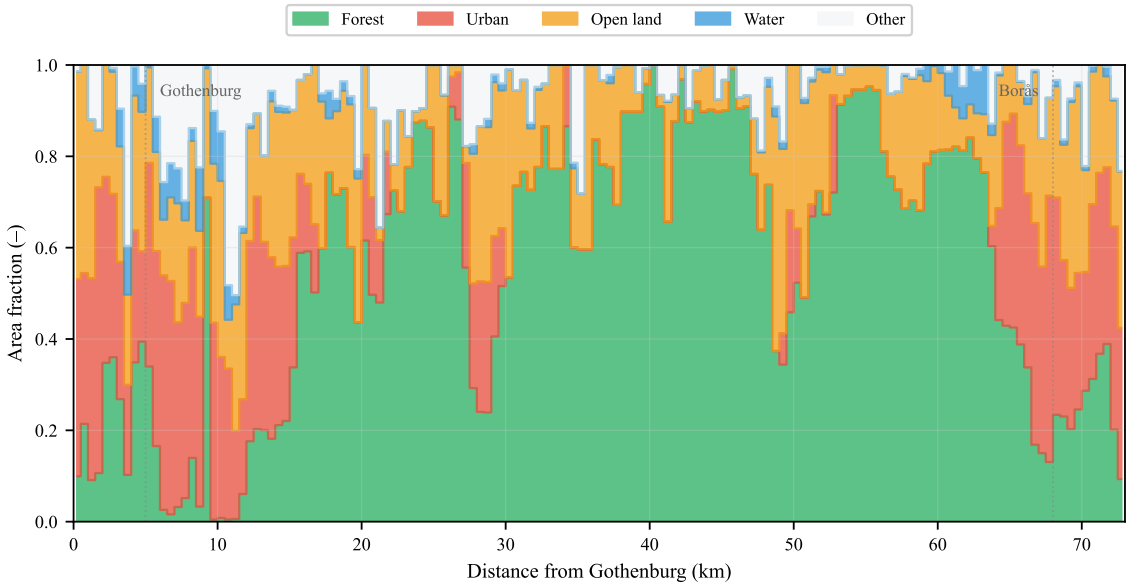


Figure 4.7: Land cover composition along a trip, aggregated into 500 m distance bins. Area fractions are computed within a 250 m radius buffer around each segment centre from Lantmäteriet Marktäcke data.

Table 4.2: Mean land-cover area fractions within a 250 m buffer around road segments, aggregated into 5km distance bins along RV 40.

Distance (km)	$n_{\mathbf{seg}}$	**Forest (–)**	**Water (–)**	**Open (–)**	**Urban (–)**	$\overline{SR}$ (–)
0–5	10	0.323	0.058	0.268	0.351	1.522
5–10	10	0.344	0.109	0.230	0.318	1.196
10–15	10	0.395	0.031	0.287	0.286	1.182
15–20	10	0.556	0.052	0.275	0.117	1.146
20–25	10	0.694	0.011	0.168	0.126	1.109
25–30	10	0.626	0.026	0.217	0.131	0.928
30–35	10	0.714	0.018	0.208	0.061	0.934
35–40	10	0.695	0.025	0.209	0.072	0.910
40–45	10	0.780	0.011	0.149	0.059	0.962
45–50	10	0.651	0.036	0.228	0.084	1.026
50–55	10	0.613	0.018	0.231	0.138	1.114
55–60	10	0.536	0.043	0.249	0.171	1.103
60–65	10	0.527	0.072	0.187	0.214	1.205
65–70	10	0.290	0.039	0.284	0.387	1.551
Route mean		*0.553*	*0.039*	*0.228*	*0.180*	*1.135*

4.2.2.4 Road Segments Land-Cover Analysis

To further interpret the spatial variation observed in the wind conditions of different road segments, the local geographic environment surrounding each road segment

was examined using GIS-based land-cover data. This analysis aimed to determine whether road segments with different local wind behaviors were located in systematically different environmental surroundings.

As described in the Methods chapter, the study route was divided into 500 m road segments based on the distance traveled by the truck. For each segment, a circular buffer with a radius of 250 m was constructed around the segment center to characterize the immediate surrounding environment that is most likely to influence the local wind field. The 250 m radius was chosen as a practical spatial scale that captures nearby land-cover conditions while limiting the inclusion of more distant features that are less representative of the local road environment. No formal sensitivity analysis of the buffer radius was performed, and the selected value should therefore be regarded as a modeling choice rather than an optimized parameter.

For each segment, a circular buffer with a radius of 250 m was constructed around the segment center to characterize the surrounding environment. The area fractions of the reclassified land-cover categories within each buffer were then calculated. A road segment was assigned to a dominant environment class only when one land-cover category occupied at least 50% of the buffer area. Segments for which no single category reached this threshold were classified as Mixed. The 50% threshold was used to ensure that the assigned class represented the majority of the surrounding land-cover composition rather than only the largest among several similarly represented categories.

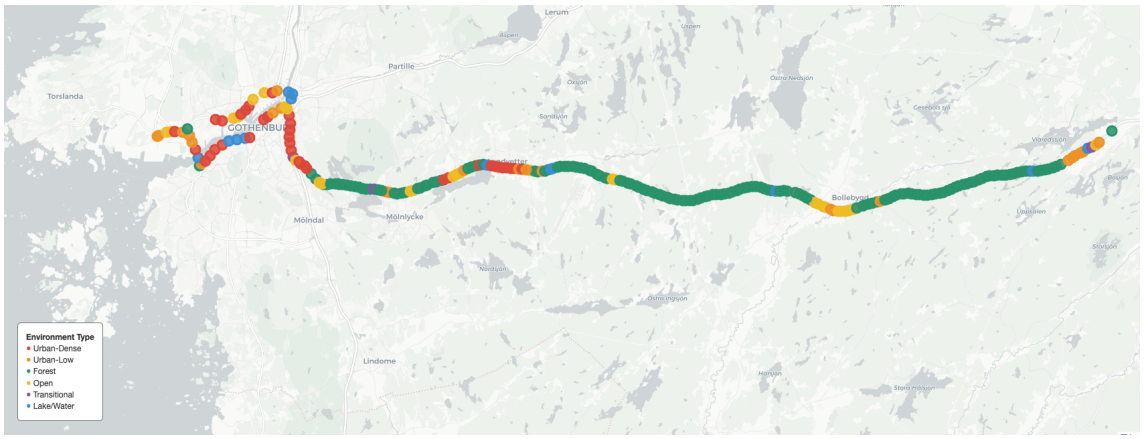


Figure 4.8: Overview of road-segment classification in the main land-cover type of the route from Gothenburg to Borås.

Figures 4.9 and Figure 4.10 present the color classification of the type of land-cover along the route. Urban-dense and urban-low environments dominate the central Gothenburg road network, whereas forest and open-land segments occur more frequently toward the outer parts of the area and the highway along RV 40. Transportation-related environments are mainly associated with major road infrastructure and industrial areas, while fewer segments are classified as water-dominated or transitional environments. The map therefore shows that the route contains substantial spatial variation in its surrounding surface characteristics rather than a single homogeneous landscape type.

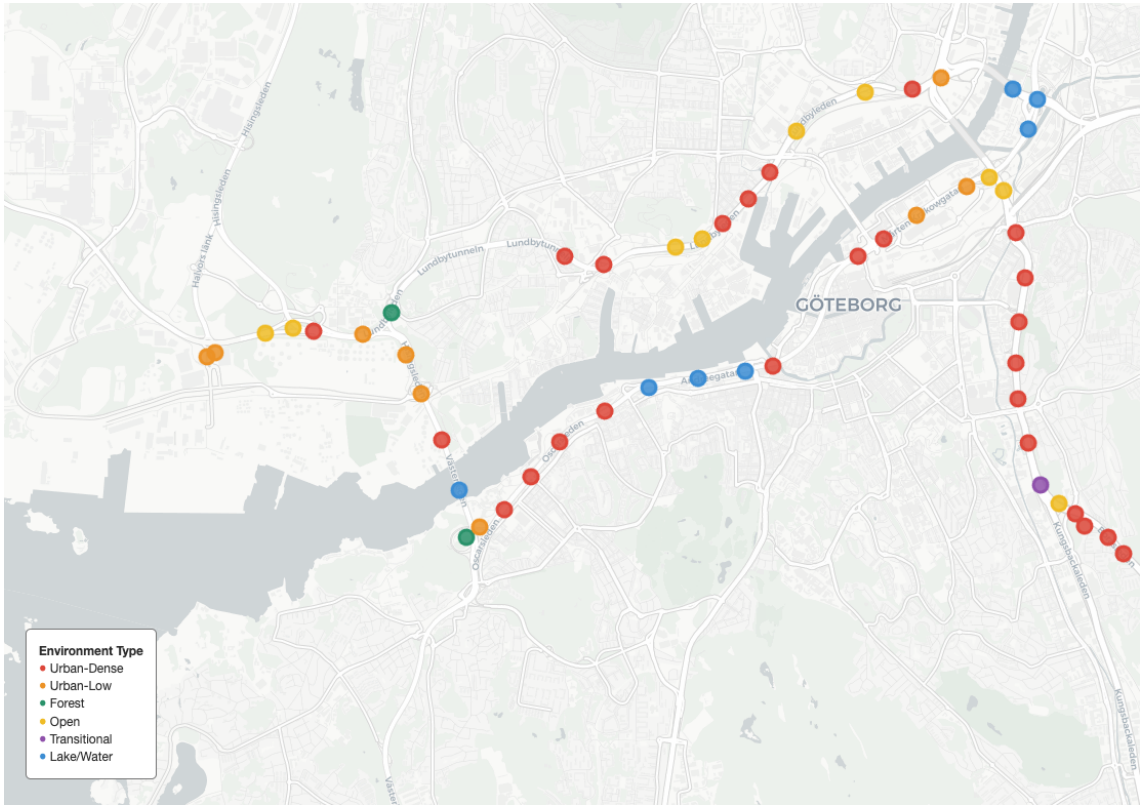


Figure 4.9: Dominant land-cover type assigned to each 500-meter road segment around the Gothenburg city area.

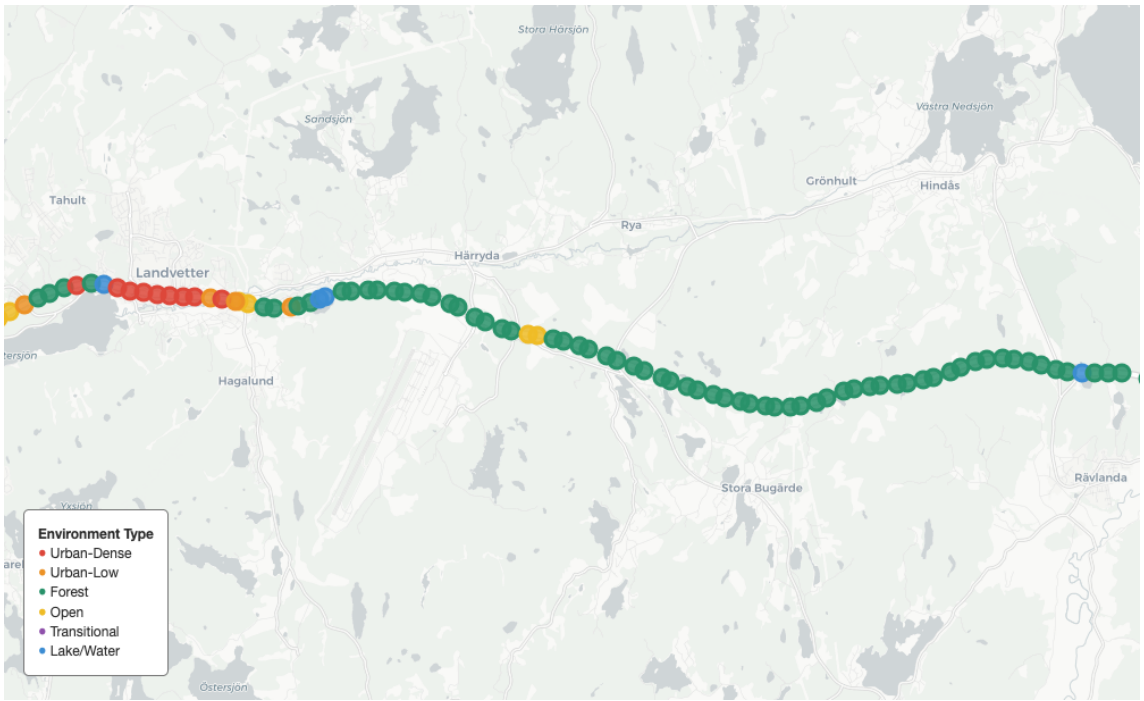


Figure 4.10: Dominant land-cover type assigned to each 500-meter road segment along the highway from Landvetter Airport to Borås.

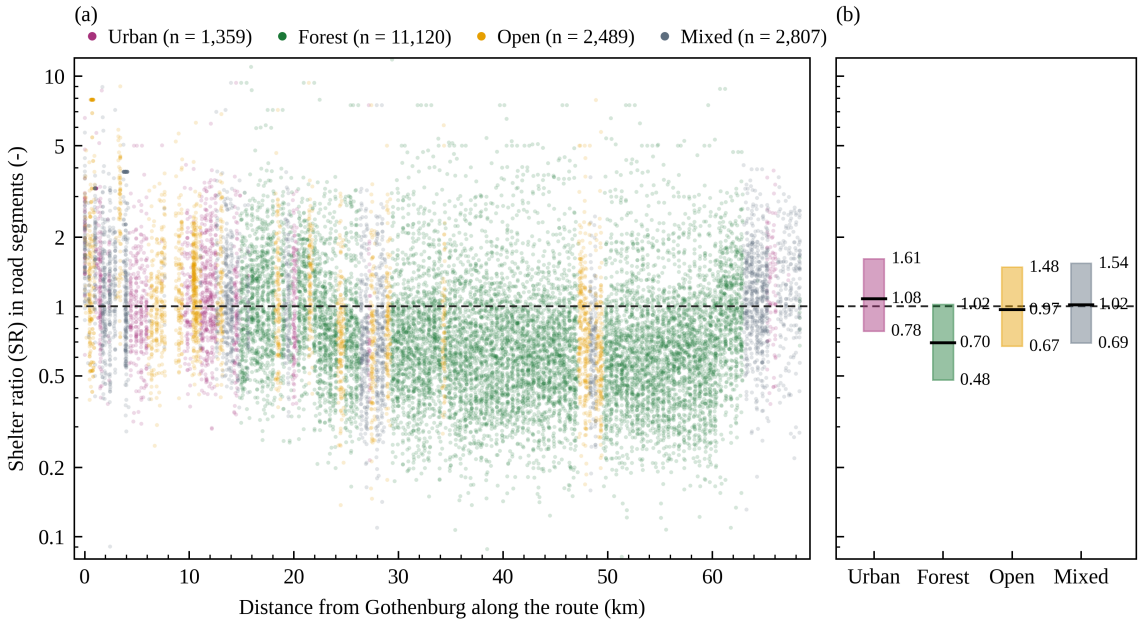


Figure 4.11: Shelter ratio of individual road-segment observations along the route, stratified by segment type. (a) All $n = 18{,}678$ valid segment–trip observations from 143 trips in both travel directions. (b) Median (black line) and interquartile range (shaded bar) of SR for each segment type, with the 75th percentile, median, and 25th percentile given numerically. Segment types are defined by areal dominance ($\geq 50\%$) of the corresponding land-cover class within the segment buffer; segments without a dominant class are labeled Mixed.

Figure 4.11(a) presents all valid segment–trip observations for road segments assigned to the land-cover categories used in this analysis. Each point represents the shelter ratio (SR) observed for one road segment during one trip, together with its location along the route.

Figure 4.11(b) summarizes the same dataset using the median and interquartile range for each road-segment type, enabling a direct comparison of their central tendencies and variability. Forest-dominated segments exhibit the lowest wind-speed ratios, with a median SR of 0.70 and an interquartile range of 0.48–1.02; moreover, 73.8% of these observations have $SR < 1$. Urban or built-up segments show the highest ratios, with a median SR of 1.08 and an interquartile range of 0.78–1.61, while 56.7% of the observations have $SR > 1$. Open and mixed segments lie between these two categories and are closer to the neutral condition, with median SR values of 0.97 and 1.02, respectively.

These results indicate contrasting local effects on the regional wind field. In urban segments, the locally measured wind speeds are, on average, higher than those reported by the meteorological stations, whereas in forest-dominated highway segments they are generally lower. Because these segment types are spatially concentrated in different parts of the route rather than randomly distributed, road-segment type, route location, and local wind conditions are closely related. Overall, the results show that the same synoptic-scale wind can be attenuated to approximately 70% of the reference value across much of the route while being locally intensified near the more urbanized ends of the route. The surrounding land-cover type therefore appears to be an important factor in determining whether regional wind is attenuated or amplified at the road-segment level.

4.2.2.5 Layer 3: Segment Residual Correction

After accounting for the regional wind-speed correction and the recurring wind patterns shared by clusters of road segments in Layers 1 and 2, systematic residual differences remain for some individual segments. These differences may be associated with highly localized effects, including gaps in vegetation, building-induced flow channeling, exposure to open water, roadside structures, and other site-specific features that are not fully captured by either the global correction or the cluster-level representation.

Layer 3 therefore estimates a segment-specific mean residual from repeated observations. Rather than representing short-term turbulence or random gusts, this term is intended to capture a location-specific bias that recurs across trips. It can improve predictions for unseen trips along the same route; however, because the correction is estimated separately for each segment, it is inherently route-specific and cannot be directly transferred to road segments that were not represented in the training data.

Layer 3 was evaluated using road segments for which repeated Layer 2 residual observations were available across multiple trips. In total, 456 road segments were included in the segment-level residual analysis.

For each analyzed road segment, a one-sample t-test was applied to the Layer 2 residuals to test the null hypothesis that the mean residual was zero. This significance test was used as a diagnostic analysis of the persistence of segment-level bias, rather than as a criterion for whether the Layer 3 correction was applied. Segments with $p < 0.05$ were interpreted as showing statistically detectable evidence of a non-zero mean residual. Of the 456 analyzed segments, 136 showed a significant non-zero mean residual, while 320 did not.

The spatial distribution of the segment-level residuals along the route is shown in Figure 4.12, where statistically significant non-zero residuals are highlighted separately from non-significant segments.

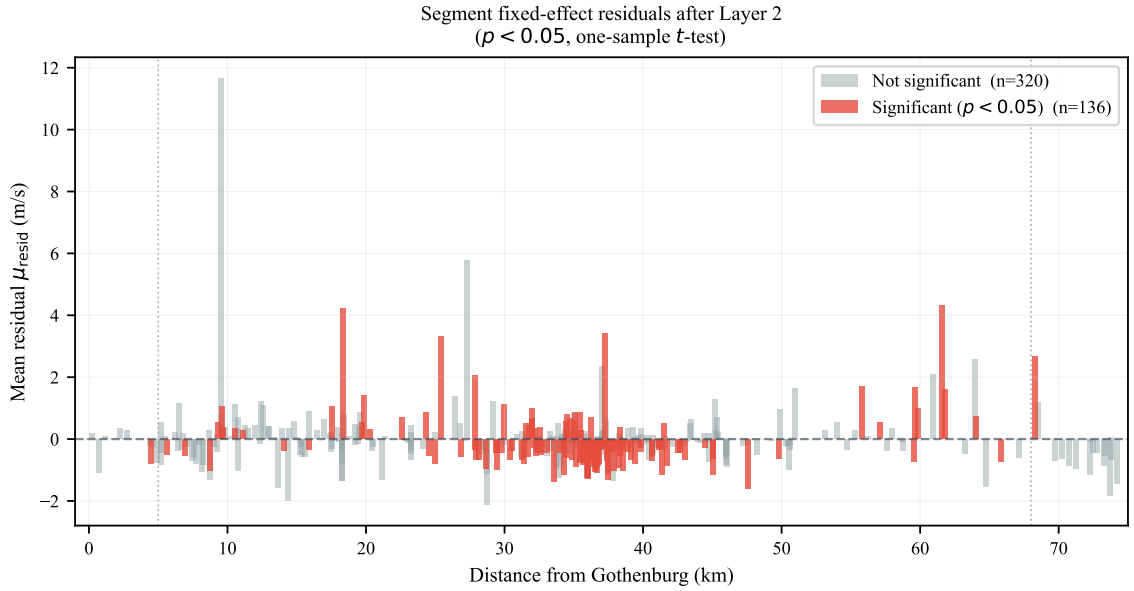


Figure 4.12: Segment-level mean residuals after Layer 2 correction, plotted against distance from Gothenburg.

4.2.2.6 Model Validation and Generalization

The complete three-layer model is expressed as:

$$\hat{V}_{L3}(k,i) = 2.464\, V_{\mathrm{SMHI}}(k,i)^{0.280} + \Delta_{c(k)} + \mu_{\mathrm{resid}}^{(-i)}(k) \tag{4.9}$$

The three-layer model substantially reduces the systematic bias in the SMHI baseline, narrowing the error distribution and centering it closer to zero (Figure 4.13). Prediction error was defined as $e = \hat{V} - V_{\mathrm{anem}}$. The SMHI baseline shows a negative mean error, indicating systematic underprediction, whereas the corrected model is approximately unbiased and exhibits substantially lower error dispersion.

The monthly results in Figure 4.14 show that the three-layer model outperforms the SMHI baseline in every month shown, with improvements ranging from about 31% to 51%. This indicates that the correction is not restricted to a particular season. However, the improvement varies by month, which may reflect differences

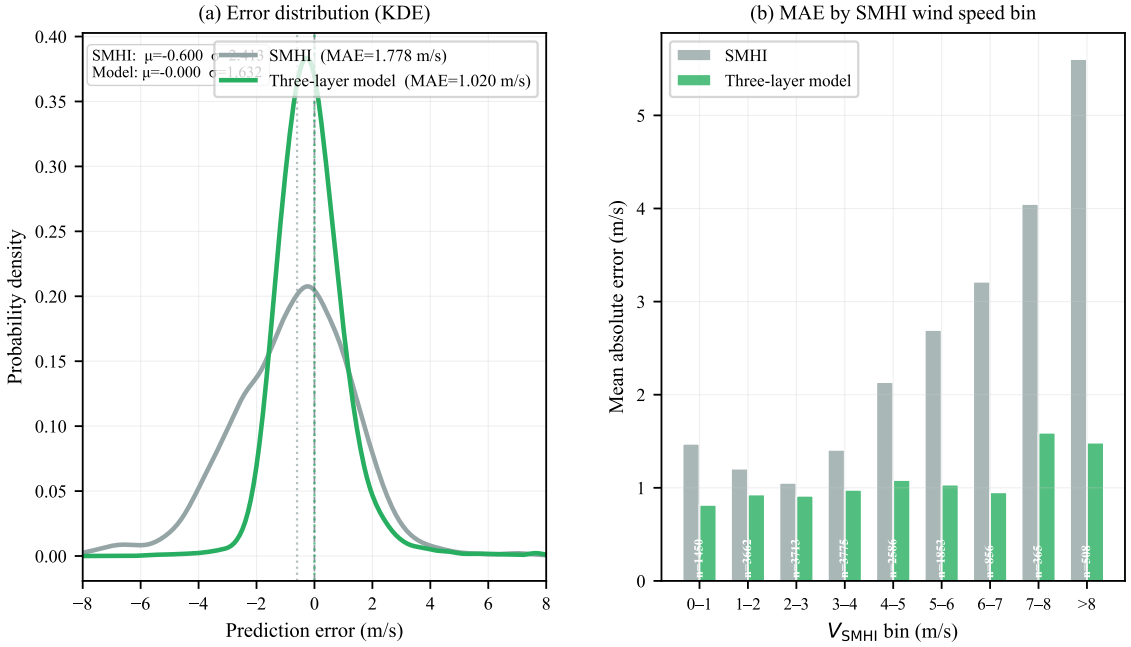


Figure 4.13: (a) Kernel density estimates of prediction error for the SMHI baseline and three-layer model. (b) Mean absolute error stratified by SMHI wind speed bin.

in prevailing wind conditions, sample size, and the distribution of trips and wind directions.

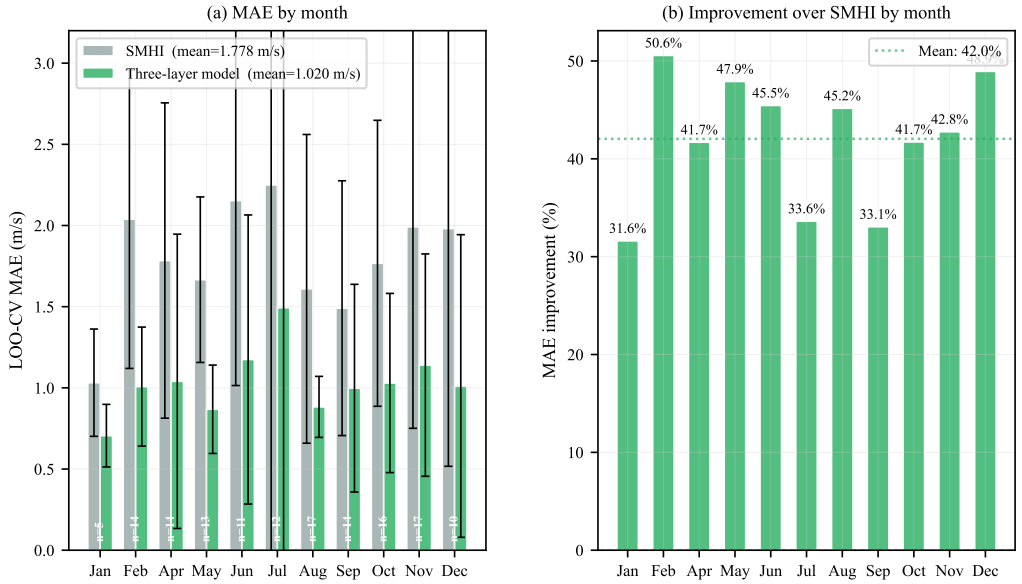


Figure 4.14: (a) Monthly LOO-CV MAE for the SMHI baseline and three-layer model. Error bars indicate one standard deviation across trips within each month. (b) Monthly improvement of the three-layer model over the SMHI baseline.

4.2.3 Integrated Model

To integrate the "Topographic model" and the "Landscape model" the results from the topographic model were plugged into the landscape model with the third layer removed. The third layer was removed because the residual metric would overfit the model to our specific road. A result for the wind angle model is presented in Figure A.4.



Figure 4.15: Results for models in the angle section around 90 degrees.

To compare the elevation model and the integrated model, Table 4.3 presents the mean absolute errors for both models compared with the measurements.

4.2.4 Wind Direction Model

The model for calculating the local average wind angle (in degrees) on the road section was determined as:

$$\begin{aligned}\theta = {} & 2.149 \cdot 10^{-9}\theta_{\text{SMHI}}^5 - 1.946 \cdot 10^{-6}\theta_{\text{SMHI}}^4 + 6.114 \cdot 10^{-4}\theta_{\text{SMHI}}^3 \\ & - 7.642 \cdot 10^{-2}\theta_{\text{SMHI}}^2 + 3.982\,\theta_{\text{SMHI}} + (\beta - 90)\end{aligned} \tag{4.10}$$

Since the wind direction is such a noisy measurement, the best way was found to model it using a very general method to avoid overfitting. The model assumes that regional wind directions within an angle section are uniformly distributed. The polynomial part of the wind direction model is a general part that dictates how the wind speed from SMHI is affecting the local wind speed while the offset $\beta - 90$ shifts the polynomial to be aligned with the correct road heading. The measured angles for sections 0 and 330 were set to the same value for the regression because the section 0 and 330 measurements were outliers due to an insufficient sample size.

Table 4.3: Absolute errors by angle (rounded to 2 decimals).

Angle section [deg]	Topographical model [m/s]	Integrated model [m/s]
0	1.11	0.82
30	1.17	0.78
60	0.98	0.79
90	1.11	1.00
120	0.91	0.84
150	1.59	1.04
180	0.78	0.63
210	0.90	0.77
240	1.15	0.91
270	1.09	0.94
300	1.36	0.95
330	1.10	0.81
Averages:	1.11	0.86

Figure 4.16 shows the points (x= section angle, y= average measurement angle) and the regressed polynomials from degree 1 to 5.

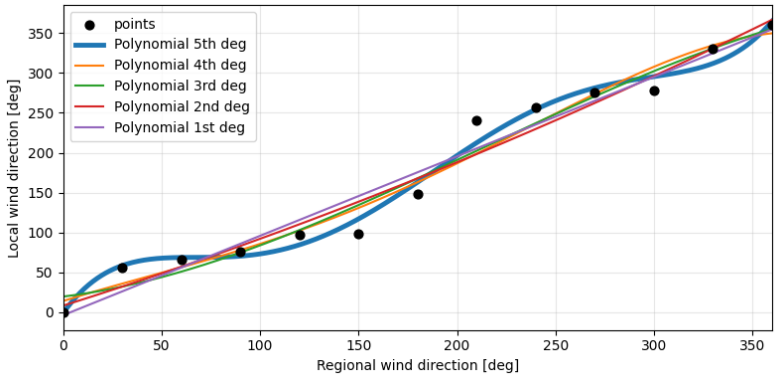


Figure 4.16: Polynomial comparison for wind direction model.

Table 4.4 presents the used points as well as the average absolute error between the model and the measurements on all 500 meter long sections. The results for the wind direction model in sections 0 and 330 should be disregarded because the sample size was insufficient.

4.3 Rolling Resistance

The results from the rolling resistance model are presented and discussed.

Section angle	Measured angle	Absolute error
0	0	65.7
30	56	38.00
60	66	23.79
90	76	18.57
120	97	23.21
150	98	34.15
180	148	7.22
210	240	22.88
240	257	24.11
270	275	25.01
300	278	37.18
330	330	120.30
Average:	-	36.68

Table 4.4: Section angle and measured angle.

4.3.1 Rolling Resistance Model

With the rolling resistance model applied to a cold and dry trip, respectively a hot and dry trip, it is visible that the model performs better in a cold climate. The resulting states $x = [T_{TB}, T_{TA}]$ are plotted and shown in Figures 4.17 and 4.18.

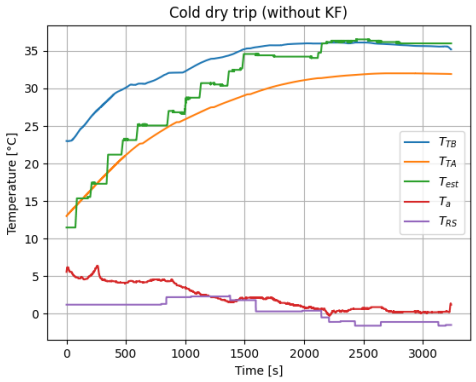


Figure 4.17: Cold dry trip.

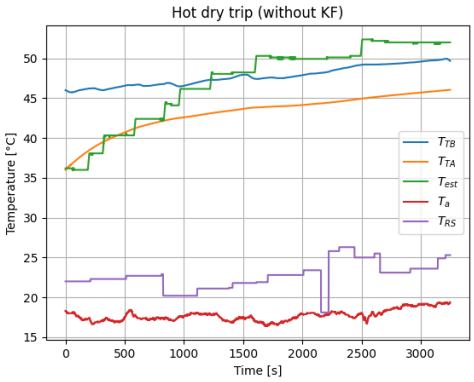


Figure 4.18: Hot dry trip.

When comparing T_{TA} and T_{est} (which should be congruent) in the plots, it is observable that T_{TA} has a more realistic shape in the cold trip. One reason for this could be that the model does not account for the fact that hot weather often indicates sun which can increase the road surface temperature can be significantly higher than the air temperature. This is visible in the plot, the T_{RS} measurement is hotter than T_a. The plot for the hot trip strengthens this claim by reaching steady state at a too low temperature since the model was not developed in that condition as a possibility.

Figures 4.19 and 4.20 plot the results for the rolling resistance model when applied

to trips on rainy days. The model performs best on the cold trip. On the hot trip, the model heavily underestimates the temperature created in the tire. It is possible that the road has already dried on the trip, thus removing the cooling effect from the water on the road that the model assumes.

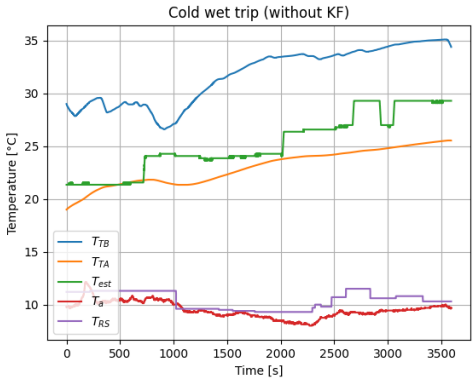


Figure 4.19: Cold wet trip.

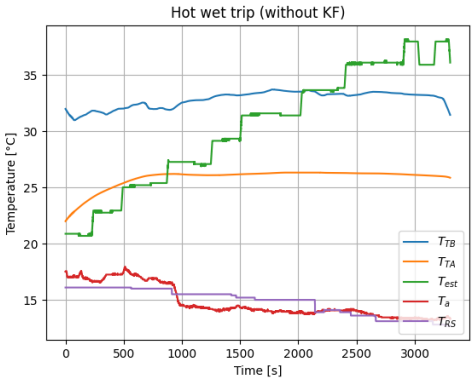


Figure 4.20: Hot wet trip.

4.3.2 Rolling Resistance Model with Observer

Figures 4.21 to 4.24 show the previous cases with a Kalman filter applied to the model. All cases perform well except the hot rainy trip. Even with the Kalman filter, the model cannot be fully corrected to match the measurements. While it is possible that a different tuning could improve this case, multiple iterations did not identify suitable parameters. To make the model perform better, it would be wise to integrate measurements of the current road condition to get the correct c_{RS}.

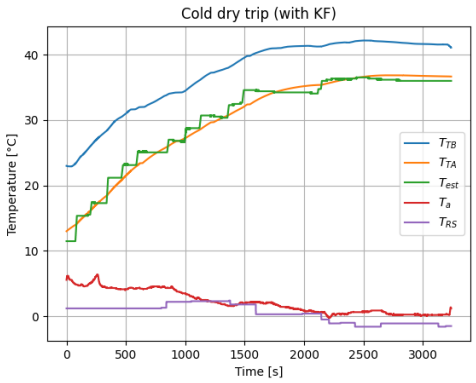


Figure 4.21: Cold dry trip with KF.

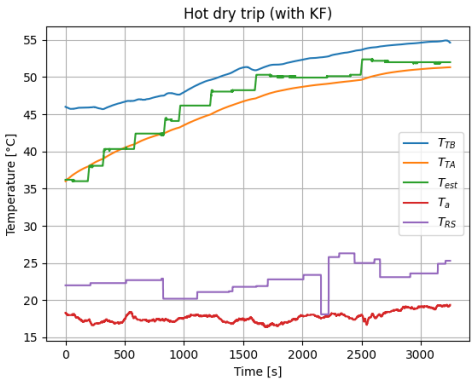


Figure 4.22: Hot dry trip with KF.

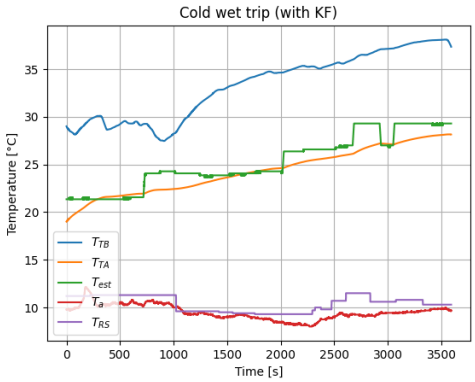


Figure 4.23: Cold wet trip with KF.

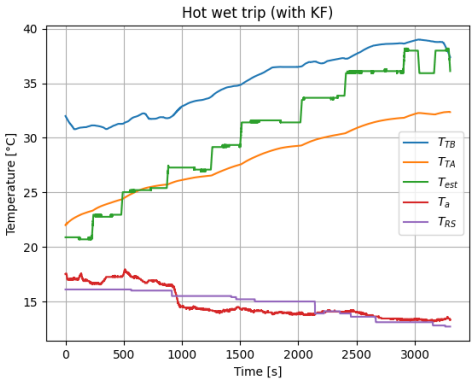


Figure 4.24: Hot wet trip with KF.

The importance of the Kalman filter highlights the advantages of comparing and updating with real measurements which should be passed on to the final energy consumption model.

5

Conclusion

The wind sensor calibration was performed on a controlled test track to isolate sensor-specific distortions from the true ambient wind, yielding coefficients for the headwind and crosswind components that correct for aerodynamic distortion caused by the cab geometry. A separate validation with a different wind visor setting gave consistent results.

All model parameters were derived from a single route between Gothenburg and Viared, which covers a representative mix of forest, open land, and urban terrain but has a predominantly east-west orientation and mostly flat topography. The power law correction is expected to transfer to other routes, as it reflects a bias in the SMHI station network rather than route-specific geometry. The cluster correction should transfer to routes with similar land cover, provided the same Lantmäteriet data are used. For this reason, segment residuals do not transfer and are excluded from the integrated model. Cross-route validation is necessary before deploying the model for fleet-scale range prediction.

Topography was found to be a major factor for wind speed; a simple model based only on it could reduce the average absolute error by 0.7 m/s compared with the SMHI prediction. High areas block the wind, while low areas let it pick up speed. Another important factor is landscape type; open landscapes will have higher wind speeds, while forests will restrict wind flow. The biggest differences compared with regional wind measurements will occur in forest areas blocked by high mountains, since weather stations are mostly placed in high, open areas.

The wind direction model achieves a mean absolute angle error of 36.68° (24.41° when disregarding sections 0 and 330), considerably larger than the wind speed error. This reflects the noisy nature of wind direction: even under similar regional conditions, the instantaneous local direction varies substantially between trips, and the fifth-degree polynomial captures only the average statistical relationship between regional and local direction. Wind direction therefore adds more uncertainty to aerodynamic drag estimates than wind speed, especially at large yaw angles where the drag coefficient is most sensitive.

The two-state tire temperature model was evaluated on a cold dry trip and a hot dry trip. It produces more realistic cavity air temperature behavior in the cold trip, where the estimated T_{TA} aligns closely with the TPMS measurement. In the hot

trip, the model reaches steady state at too low a temperature. A likely cause is solar radiation: in warm weather, the road surface temperature exceeds the ambient air temperature, as seen in the measured T_{RS} being higher than T_a in the hot trip. The model uses T_a and T_{RS} as disturbance inputs but does not model the radiative heating behind this difference, which limits accuracy in summer conditions. In winter and overcast conditions, where T_{RS} tracks T_a more closely, the model is expected to perform better, and this is the primary regime of interest for cold-weather range prediction. Adding an observer in the form of a Kalman filter significantly improves the model but also has limitations in how much it can correct the model to the measurement.

Overall, the results support the thesis's central motivation: accounting for local road weather is necessary for accurate aerodynamic drag estimation. Using SMHI data directly introduces a mean absolute error of 1.778 m/s in wind speed, which, at a cruising speed of about 25 m/s, produces a non-trivial uncertainty in drag force because drag depends quadratically on relative air speed. The integrated model reduces this error by 48.4% using only publicly available inputs and no additional on-vehicle sensors. The rolling resistance model also shows that tire temperature, and thus rolling resistance, differs significantly between warm and cold conditions, and the observer provides a path to temperature-aware rolling resistance estimation using existing TPMS hardware.

Further Research

This project still has a lot of ground to cover in order to be usable in an energy consumption model. First, the data calibration and model must be validated on other roads in different landscapes and headings. The prediction model then needs to be integrated with a CFD model to calculate the predicted air-drag force. The air drag force and the rolling resistance from the model will then be added to the energy consumption model. The model will also need a sensitivity analysis of section length to see whether results differ for lengths other than 500 meters.

Regarding energy consumption models, this study produces two inputs: a local wind field model and a temperature-dependent rolling resistance coefficient. These two models, along with CFD-derived drag maps and vehicle powertrain efficiency, can then be assembled into a complete energy consumption model, and the end-to-end energy consumption prediction accuracy can be verified in practice.

The data source is limited to model parameters from a single route in the RV 40 region. Future studies could expand the data range and further validate the model's applicability.

For rolling resistance, a prediction model for the local temperature could also be developed. However, temperature is generally more stable, and a simple interpolation model with a small bias towards a variable such as altitude would probably be sufficient.

Bibliography

[1] "Road transport – Breakthrough Agenda Report 2025 – Analysis."

[2] M. Askerdal, J. Fredriksson, and L. Laine, "Development of simplified air drag models including crosswinds for commercial heavy vehicle combinations," *Vehicle System Dynamics*, vol. 62, no. 5, pp. 1085–1102, 2024.

[3] J. Zhang, Z. Wang, P. Liu, and Z. Zhang, "Energy consumption analysis and prediction of electric vehicles based on real-world driving data," *Applied Energy*, vol. 275, p. 115408, 2020.

[4] C. D. Cauwer, J. V. Mierlo, and T. Coosemans, "Energy Consumption Prediction for Electric Vehicles Based on Real-World Data," *Energies*, vol. 8, no. 8, pp. 8573–8593, 2015.

[5] D. Martini, S. M. Miraftabzadeh, N. Matera, M. Longo, and S. Leva, "Evaluation of electric vehicle consumption models based on real-world driving data," *International Journal of Electrical Power & Energy Systems*, vol. 172, p. 111116, 2025.

[6] Q. Zhu, Y. Huang, C. Feng Lee, P. Liu, J. Zhang, and T. Wik, "Predicting electric vehicle energy consumption from field data using machine learning," *IEEE Transactions on Transportation Electrification*, vol. 11, no. 1, pp. 2120–2132, 2025.

[7] T. Gillespie, *Fundamentals of Vehicle Dynamics*. SAE International, 2021.

[8] Z. Mohamed-Kassim and A. Filippone, "Fuel savings on a heavy vehicle via aerodynamic drag reduction," *Transportation Research Part D: Transport and Environment*, vol. 15, no. 5, pp. 275–284, 2010.

[9] D. Komnos, S. Broekaert, T. Grigoratos, L. Ntziachristos, and G. Fontaras, "In use determination of aerodynamic and rolling resistances of heavy-duty vehicles," *Sustainability*, vol. 13, no. 2, 2021.

[10] T. Curry, I. Liberman, L. Hoffman-Andrews, and D. Lowell, "Reducing aerodynamic drag and rolling resistance from heavy duty trucks: Summary of available technologies and applicability to chinese trucks," *MJ Bradley and Associates LLC, California*, 2012.

[11] F. Cheli, P. Belforte, S. Melzi, E. Sabbioni, and G. Tomasini, "Numerical–experimental approach for evaluating cross-wind aerodynamic effects on heavy vehicles," *Vehicle System Dynamics*, vol. 44, no. sup1, pp. 791–804, 2006.

[12] R. Abel, L. Pegel, and A. Waldmann, "On the importance of highly resolved wind forecasts for range estimation," in *22. Internationales Stuttgarter Symposium* (M. Bargende, H.-C. Reuss, and A. Wagner, eds.), (Wiesbaden), pp. 187–196, Springer Fachmedien Wiesbaden, 2022.

[13] C. Baker, "A simplified analysis of various types of wind-induced road vehicle accidents," *Journal of Wind Engineering and Industrial Aerodynamics*, vol. 22, no. 1, pp. 69–85, 1986.

[14] J. Ejsmont, S. Taryma, G. Ronowski, and B. Swieczko-Zurek, "Influence of temperature on the tyre rolling resistance," *International Journal of Automotive Technology*, vol. 19, no. 1, pp. 45–54, 2018.

[15] G. Descornet, "Road-Surface Influence on Tire Rolling Resistance," in *Surface Characteristics of Roadways: International Research and Technologies* (g.-i. family=Meyer, given=WE and J. Reichert, eds.), vol. STP1031-EB, p. 0, ASTM International, 1990.

[16] M. Askerdal, F. Bruzelius, and J. Fredriksson, "Effects of external tire heating on rolling resistance energy consumption," in *16th International Symposium on Advanced Vehicle Control* (G. Mastinu, F. Braghin, F. Cheli, M. Corno, and S. M. Savaresi, eds.), (Cham), pp. 29–35, Springer Nature Switzerland, 2024.

[17] Y.-J. Lin and S.-J. Hwang, "Temperature prediction of rolling tires by computer simulation," *Mathematics and Computers in Simulation*, vol. 67, no. 3, pp. 235–249, 2004.

[18] J. Song, "Evaluation of driving resistance and energy consumption in electric vehicles under various ambient and tire temperatures using real-world driving data," *eTransportation*, vol. 25, p. 100454, 2025.

[19] H. Jansson and M. Åsenius, "The relation between rolling resistance and tyre temperature in real driving scenarios," 2021.

[20] Lantmäteriet, "Marktäcke nedladdning, vektor." Accessed: Sep. 14, 2026. [Online]. Available: `https://www.lantmateriet.se/sv/geodata/vara-produkter/produktlista/marktacke-nedladdning-vektor/`.

[21] Lantmäteriet, "Byggnad nedladdning, vektor." Accessed: Sep. 14, 2026. [Online]. Available: `https://geotorget.lantmateriet.se/dokument/projects/byggnad-nedladdning-vektor/released/2025.02/`.

[22] Lantmäteriet, "Markhöjdmodell nedladdning." Accessed: Sep. 14, 2026. [Online]. Available: `https://www.lantmateriet.se/sv/geodata/vara-produkter/produktlista/markhojdmodell-nedladdning/`.

[23] J. Wieringa, "Roughness-dependent geographical interpolation of surface wind speed averages," *Quarterly Journal of the Royal Meteorological Society*, vol. 112, no. 473, pp. 867–889, 1986.

[24] B. Zhao *et al.*, "Investigation of exposure correction models for wind speed measurements," *Meteorological Applications*, vol. 29, 2022.

[25] D. R. Roberts, V. Bahn, S. Ciuti, M. S. Boyce, J. Elith, G. Guillera-Arroita, S. Hauenstein, J. J. Lahoz-Monfort, B. Schröder, W. Thuiller, D. I. Warton, B. A. Wintle, F. Hartig, and C. F. Dormann, "Cross-validation strategies for data with temporal, spatial, hierarchical, or phylogenetic structure," *Ecography*, vol. 40, no. 8, pp. 913–929, 2017.

A

Appendix 1



Figure A.1: Results for models in angle section around 0 degrees.

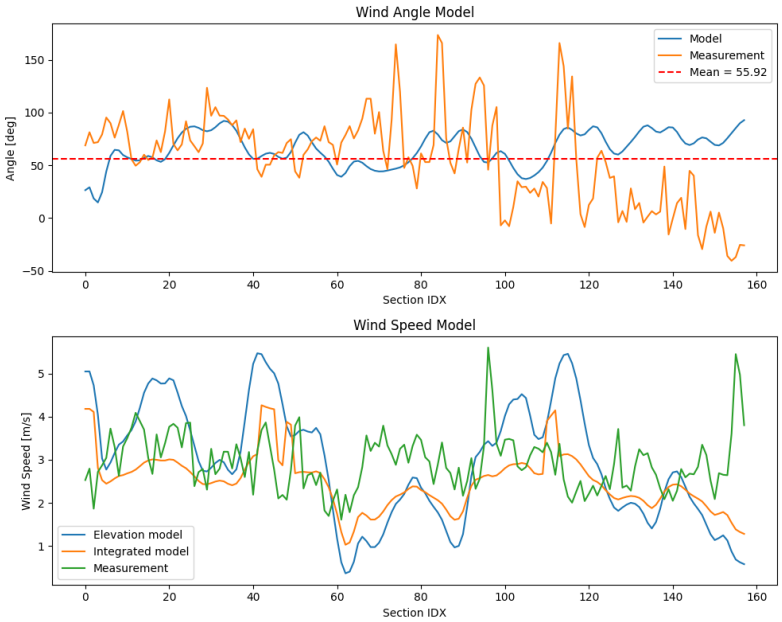


Figure A.2: Results for models in angle section around 30 degrees.



Figure A.3: Results for models in angle section around 60 degrees.



Figure A.4: Results for models in angle section around 120 degrees.

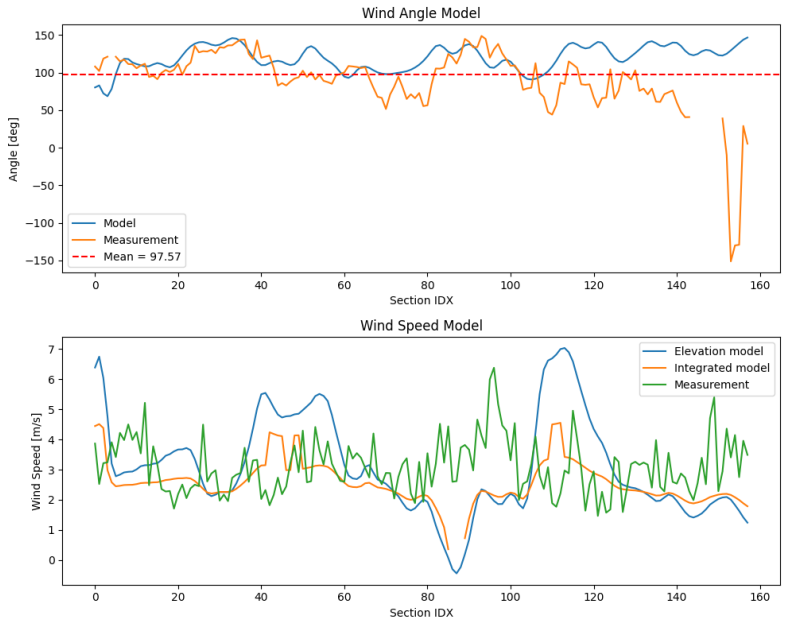


Figure A.5: Results for models in angle section around 150 degrees.

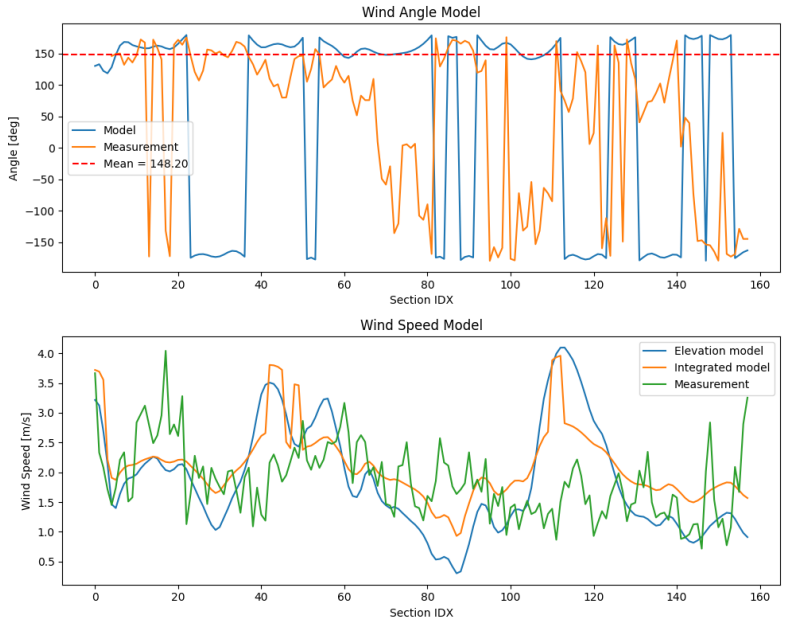


Figure A.6: Results for models in angle section around 180 degrees.

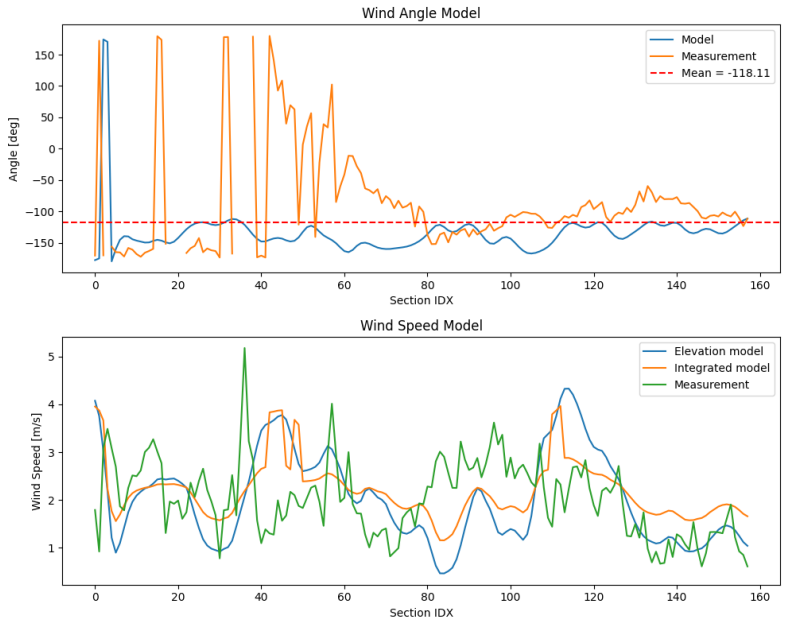


Figure A.7: Results for models in angle section around 210 degrees.



Figure A.8: Results for models in angle section around 240 degrees.



Figure A.9: Results for models in angle section around 270 degrees.

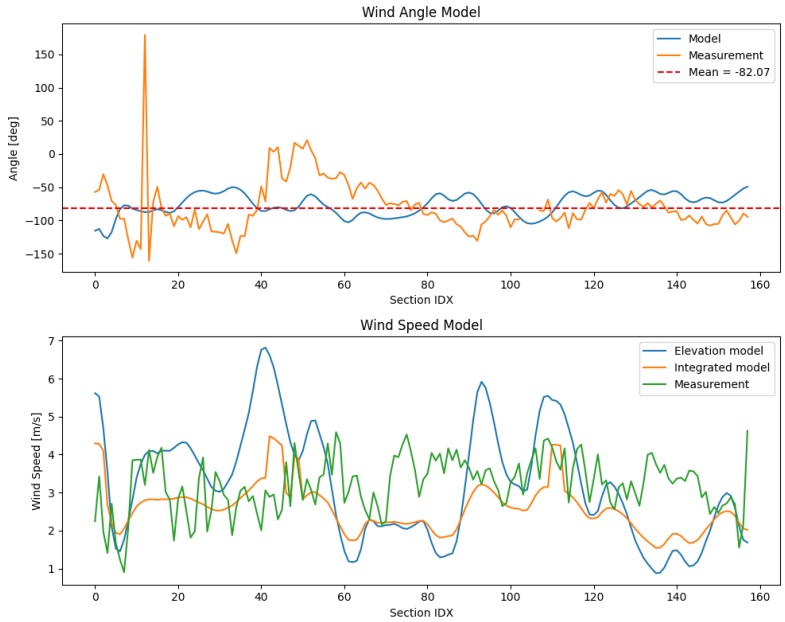


Figure A.10: Results for models in angle section around 300 degrees.



Figure A.11: Results for models in angle section around 330 degrees.

DEPARTMENT OF ELECTRICAL ENGINEERING
CHALMERS UNIVERSITY OF TECHNOLOGY
Gothenburg, Sweden
www.chalmers.se



CHALMERS
UNIVERSITY OF TECHNOLOGY